Coherent Tropical Indo-Pacific Interannual Climate Variability

CLAUDIA E. WIENERS, WILL P. M. DE RUIJTER, WIM RIDDERINKHOF,
ANNA S. VON DER HEYDT, AND HENK A. DIJKSTRA

*Institute for Marine and Atmospheric Research Utrecht, Department of Physics and Astronomy,
Utrecht University, Utrecht, Netherlands*

ABSTRACT

A multichannel singular spectrum analysis (MSSA) applied simultaneously to tropical sea surface temperature (SST), zonal wind, and burstiness (zonal wind variability) reveals three significant oscillatory modes. They all show a strong ENSO signal in the eastern Pacific Ocean (PO) but also a substantial SST signal in the western Indian Ocean (IO). A correlation-based analysis shows that the western IO signal contains linearly independent information on ENSO. Of the three Indo-Pacific ENSO modes of the MSSA, one resembles a central Pacific (CP) El Niño, while the others represent eastern Pacific (EP) El Niños, which either start in the central Pacific and grow eastward (EPe) or start near Peru and grow westward (EPw). A composite analysis shows that EPw El Niños are preceded by cooling in the western IO about 15 months earlier. Two mechanisms are discussed by which the western IO might influence ENSO. In the atmospheric bridge mechanism, subsidence over the cool western IO in autumn (year 0) leads to enhanced convection above Indonesia, strengthening easterlies over the western PO, and the creation of a large warm water volume. This is essential for the creation of (EP) El Niños in the following spring–summer. In the state-dependent noise mechanism, a cool western IO favors a strong intraseasonal zonal wind variability over the western PO in early spring (year 1), which can partly be attributed to the Madden–Julian oscillation. This intraseasonal variability induces Kelvin waves, which in early spring lead to a strong warming of the eastern PO and can initiate EPw El Niños.

1. Introduction

The El Niño–Southern Oscillation (ENSO) phenomenon is among the strongest modes of interannual variability in the climate system (Philander 1990). Because of its great influence around the globe, early prediction of strong El Niño and La Niña events can be of great value to take measures to reduce damage (Zebiak et al. 2015).

The basic processes involved in ENSO are well understood and involve the response of equatorial winds on SST anomalies and subsequent changes in the upper ocean, such as a change in thermocline slope and equatorial upwelling. The ocean response can lead to a positive (Bjerknes) feedback on the SST anomalies, and the ocean adjustment due to equatorial wave processes provides a delayed negative feedback (Neelin et al. 1998; Jin 1997a,b). Meinen and McPhaden (2000) showed that a sufficiently high Pacific warm water volume (WWV; the volume of water warmer than 20°C) is relevant for the occurrence of El Niño events because in order to warm the eastern Pacific Ocean (PO), sufficient heat should be present in the western PO, which is then discharged during El Niño. Also, small-scale processes can play a role in ENSO (Kleeman 2008), in particular intraseasonal spells of westerly winds (Keen 1982), such as those provided by the Madden–Julian oscillation (MJO) (Madden and Julian 1971; Zhang 2005). "Bursts" of westerly winds over the western PO generate equatorial Kelvin waves, which affect the thermocline in the eastern PO, favoring the development of an El Niño (Kessler et al. 1995; McPhaden et al. 2006).

Two types of El Niño events have been distinguished (Ashok et al. 2007; Larkin and Harrison 2005; Kug et al. 2009; Kao and Yu 2009). One type, which we will refer to as central Pacific (CP) El Niño, is characterized by warm anomalies in the central PO, whereas eastern Pacific (EP) El Niños have the strongest warm anomalies in the eastern PO. Kao and Yu (2009) report that the CP El

---

Corresponding author address: Claudia Elisabeth Wieners, Institute for Marine and Atmospheric Research Utrecht, Dept. of Physics and Astronomy, Utrecht University, Princetonplein 5, 3584 CC Utrecht, Netherlands.
E-mail: c.e.wieners@uu.nl

Niño temperature signal reaches less deep than that of EP El Niños and suggest that CP El Niños might be more dominated by local winds and SST advection, whereas for EP El Niños thermocline processes and the WWV are important as well. Yu and Kim (2010) find that CP El Niños can occur during recharged, neutral, or discharged states of the WWV.

It has been suggested that ENSO is also influenced by processes in the neighboring Indian and Atlantic Oceans. The influence of the Atlantic Ocean appears to be small, although it has been suggested that SST anomalies in the north tropical Atlantic during boreal spring can affect ENSO occurrence (Ham et al. 2013). The Indian Ocean (IO) variability was long thought to be a passive response to ENSO (Latif and Barnett 1995), but later studies have suggested that the IO evolves to some degree independently of ENSO (Saji et al. 1999; Webster et al. 1999).

Izumo et al. (2010b) suggest that IO SST anomalies can influence large-scale wind patterns over the western PO (i.e., atmospheric bridge), which might explain the significant improvement of predictive skill of ENSO by taking the autumn Indian Ocean dipole (IOD) into account. In Santoso et al. (2012) and Annamalai et al. (2005), numerical experiments suggest that IO basinwide mode (IOBM) warming often associated with El Niño leads to easterly winds above the western PO, which in turn dampen the ongoing El Niño. Izumo et al. (2015) use a simple numerical model to reconcile the IOD and IOBM mechanisms. However, the IO might also influence the intraseasonal atmospheric variability above the PO, particularly MJO events that originate in the western IO and propagate eastward (Izumo et al. 2010a; Wilson et al. 2013). One of the regions in the IO with large interannual variability is the Seychelles dome (SD) region near 8°S, 50°E. This is a dynamically active region with a shallow thermocline, low SSTs, and strong air–sea coupling (Xie et al. 2002). While part of the interannual SD variability is attributed to Rossby waves forced in the eastern IO by ENSO (Xie et al. 2002), local effects and forcing by the Indian Ocean dipole (Tozuka et al. 2010) might also play a role.

In this paper, we revisit the coupling between SD and ENSO variability by analyzing observational data, thereby investigating links to the interaction pathways through IOD and IOBM mentioned above. Our main tool will be multichannel singular spectrum analysis (MSSA), a technique that is able to detect covarying propagating patterns of variability in fields of time series (Plaut and Vautard 1994). In section 2 we briefly describe the data and indices used in this analysis, as well as the MSSA technique. In section 3 we will show that SD SST in boreal summer–autumn (year 0) and Niño-3.4

SST in winter (year 1–2) are significantly negatively correlated and perform a test suggesting that the SD record contains information (linearly) independent from ENSO. The results of the MSSA analysis are presented in section 4 with a discussion of the spatiotemporal patterns involved. With the aid of a composite analysis, we then demonstrate that El Niño events preceded by a cool SD tend to be of the westward-growing EP-type El Niño. In section 5, two physical mechanisms will be discussed by which the SD region influences ENSO.

2. Data and methods

a. Derived data, indices, and significance tests

For this study we made use of zonal wind data, both monthly and daily, at 2.5° resolution, available for the years 1948–2013, from the NCEP–NCAR reanalysis data (Kalnay et al. 1996; NOAA/OAR/ESRL PSD 2014). We also used the monthly mean SST from HadISST at 1° resolution, available for the years 1870–2011 (Rayner et al. 2003; Met Office 2012); unless stated otherwise, SST data were used for the period 1948–2011. In addition, a monthly mean WWV time series was used from the data from the NOAA/PMEL TAO Project Office (NOAA/PMEL Tropical Atmosphere Ocean Project 2014), which is available from 1980 onward, and sea surface height (SSH) anomaly data for October 1992–August 2013 were used. This satellite altimeter product is produced and distributed by AVISO, as part of the SSALTO ground processing segment (AVISO/SSALTO 2014). The data are provided as weekly "snapshots" of the state of the ocean on a certain day. Monthly data were obtained by linearly interpolating to daily values and then taking a monthly average.

In addition to standard ENSO and IOD indices, we define an extended Seychelles dome index (SDIex) as the monthly mean SST averaged over 3°–13°S, 45°–70°E. The chosen area is slightly larger than the actual Seychelles dome region 1) to include more data points to reduce measurement errors in this data-sparse region and 2) because the SST anomalies around the SD usually extend farther north than the SD itself. We denote an index with the prefix h (e.g., hSDIex) when SSH is used for the index instead of SST. Index data and regions are defined in Table 1 and Fig. 1, respectively.

We also define a field we call burstiness, which is a measure for the intraseasonal variability of the zonal wind. It is computed at each location $\mathbf{x}$ by taking the variance over 3 months of the 5-day mean zonal wind u at 850 hPa:

$$B(\mathbf{x}, m) = \sum_{p \in P_m} [u(\mathbf{x}, p) - \bar{u}(\mathbf{x}, m, p)]^2, \qquad (1)$$

TABLE 1. Definitions of indices used in this study. All indices are computed from monthly mean data.

Quantity	Definition
IODeast	SST averaged over 10°S–0°, 90°–110°E.
IODwest	SST averaged over 10°S–10°N, 50°–70°E.
DMI	Dipole mode index; DMI = IODwest − IODeast.
IOBwest	SST averaged over 20°S–20°N, 40°–70°E.
IOBeast	SST averaged over 20°S–20°N, 70°–110°E.
BWI	Basinwide index; BWI = IOBwest + IOBeast.
SDIex	SST averaged over 3°–13°S, 45°–70°E.
AOeast	SST averaged over 5°N–5°S, 15°W–15°E.
Niño-4	SST averaged over 5°N–5°S, 160°E–150°W.
Niño-3.4	SST averaged over 5°N–5°S, 170°–120°E.
Niño-3	SST averaged over 5°N–5°S, 150°–90°W.
Niño-1+2	SST averaged over 0°–10°S, 90°–80°E.
EMI	El Niño Modoki index; EMI = EMI_A − (EMI_B + EMI_C)/2, where EMI regions A, B, and C are the SST averaged over 10°N–10°S, 165°–220°E; 5°N–15°S, 110°–70°W; and 20°N–10°S, 125°–145°E; respectively.
WWV	Warm water volume from TAO data.

where $B(\mathbf{x}, m)$ is the burstiness at $\mathbf{x}$ in month m; P_m is the set of all 5-day blocks in months $m − 1, m$, and $m + 1$; and $\bar{u}(\mathbf{x}, m, p)$ is the linear fit of u at $\mathbf{x}$ over the interval P_m. Subtracting $\bar{u}$ should remove the influence of long-term trends and using 5-day wind suppresses synoptic-scale signals. Izumo et al. (2010b) used a similar concept but with a bandpass filter and wind stress. We used 850-hPa wind because it is less sensitive to orographic effects.

In all applications of correlations, regressions, and composites, the analysis is performed for each calendar month m separately to take into account phase locking to the seasonal cycle. Anomalies Q_a of a quantity Q are computed by subtracting a background value Q_b from the data, which captures variability on time scales much longer than ENSO time scales: $Q_a(y, m) = Q(y, m) − Q_b(y, m)$, where y is the year. For the relatively short time series of WWV and the SSH data, $Q_b(y, m)$ is computed by taking the linear trend over all years, with m fixed. For other quantities, a running-mean-like technique is used in order to account for possible nonlinear trends:

$$Q_b(y, m) = \frac{\sum_{k=-y_1}^{y_2} w_k Q(y + k, m)}{\sum_{k=y_1}^{y_2} w_k}, \quad (2)$$

where $y_1 = y_2 = 10$ and $w_k = 1$ if $|k| \leq 5$, and otherwise $w_k = 1/2$. The results presented below do not strongly depend on the details of the detrending.

Unless stated otherwise, significance of quantities C obtained by correlation, regression, or composite analysis is tested in a nonparametric way by recalculating C with N_{shuf} surrogate datasets in which the years were randomly shuffled. When the true C is greater (smaller) than 100% − s/2% of the surrogate C, then C is significant at s% confidence (two tailed). A value $\tilde{N}$ for N_{shuf} is considered sufficiently large when $\tilde{N}/2$ and $\tilde{N}$ yield the same limits for C; a typical value is $N_{shuf} = 2000$.

In a composite analysis, when investigating whether a quantity Q in a set of years Y_1 differs significantly from Q in a set Y_2, the significance of the auxiliary variable is tested:

$$R \equiv \frac{1}{N_1} \sum_{i \in Y_1} Q(i) - \frac{1}{N_2} \sum_{i \in Y_2} Q(i), \quad (3)$$

where N_i is the number of years in Y_i.

b. The MSSA method

The MSSA technique (Plaut and Vautard 1994) is able to determine covarying spatiotemporal patterns in multivariate data. It is a generalization of purely spatial empirical orthogonal function (EOF) analysis and purely temporal singular spectrum analysis (SSA). Both for the calculation of the statistical modes and for the significance test against red noise, we follow Allen and Robertson (1996).

The MSSA analysis is applied to a dataset consisting of SST, zonal wind, and burstiness fields. We consider data from a band extending from 20°N to 20°S for all longitudes. The spatial resolution is 2° latitude and 4° longitude for SST, 2.5° latitude and 5° longitude for the zonal wind, and 2.5° latitude and 2.5° longitude for burstiness. The time resolution is 1 month and the window length is approximately 10 years (120 lag values). Prior to computing the MSSA modes, the data are detrended as in Eq. (2), the seasonal cycle is subtracted, and a binomial low-pass filter is applied:
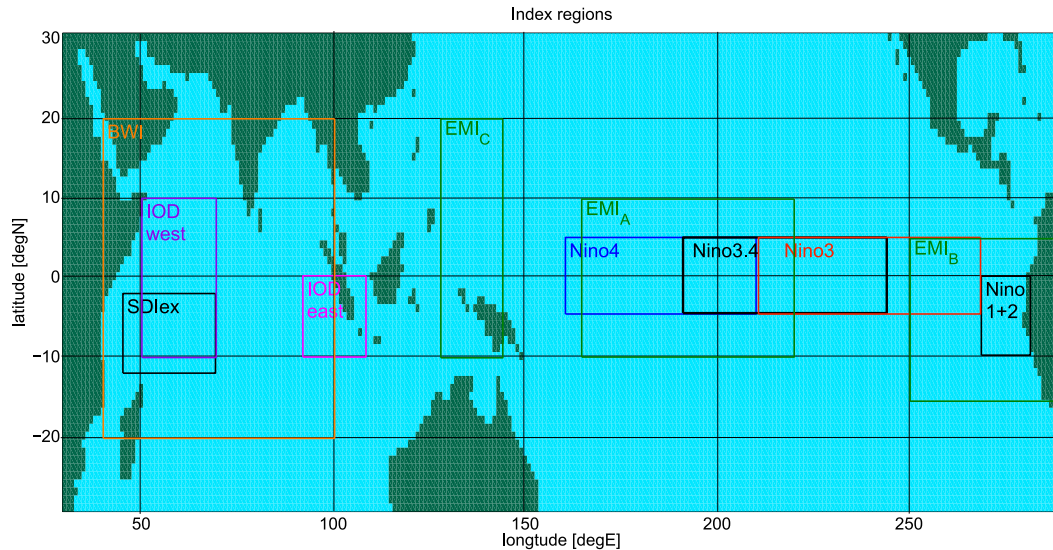
FIG. 1. Map of the areas over which the SST- and SSH-based indices are computed. Niño-4, Niño-3.4, Niño-3, Niño-1+2, SDIex, IODeast, IODwest, BWI, and EMI$_i$ are the mean of the monthly averaged SST in the corresponding box. The computation of DMI and EMI are shown in Table 1. The BWI can be split into an eastern and western half (IOBeast and IOBwest).

$$X'(t) = \frac{\sum\limits_{m=-M}^{M} a_m X(t + m\Delta t)}{\sum\limits_{m=-M}^{M} a_m} \quad \text{and}$$

$$a_m = \frac{(2M)!}{(m+M)!(M-m)!}, \tag{4}$$

where $M = 4$ and $\Delta t = 1$ month, damping signals with periods of 9 months to half of the original amplitude (Mitchell et al. 1966). The data of each of the fields are normalized by the standard deviation over space and time of each field in order to avoid the weight of the fields to depend on the units in which they are measured.

To reduce the computational effort and to obtain uncorrelated (at lag zero) data for the MSSA/significance test, the data are prefiltered by first computing ordinary EOFs over the combined dataset (Allen and Robertson 1996). The first N_{eof} EOFs (containing 90% of the variance) are selected, and the corresponding time series are used as variables in the MSSA procedure. For calculating the properties of the red noise surrogate data used in the significance test, the method described in section 4.3 of Allen and Smith (1996) is used. We will refer to the spatiotemporal patterns found by MSSA as extended EOFs (EEOFs) and the corresponding time series as principal components (PCs).

Both the data-adaptive and noise-adaptive tests described in Allen and Robertson (1996) are applied. The former serves to identify potentially significant EEOFs and their PCs, while the noise-adaptive test is used to

check whether there is really improbable high variance in the dominant frequencies of the PCs (Allen and Robertson 1996). In the significance tests, 2400 surrogate datasets were used.

3. Correlations and effects of ENSO cyclicity

In this section we show that the SD contains information linearly independent of ENSO and how the SD relates to the IOD and IOBM.

When correlating the SSH in the IO in spring–autumn (year 0) to Niño-3.4 in December (year 1; i.e., with a lag around 1.5 yr), one finds a strong negative correlation in the Seychelles dome area for April–August (Fig. 2a). For the SST data a similar signal can be found, though it is spread out over most of the western IO (not shown). A negative correlation between SDIex in August–October and Niño-3.4 in the next year's July–January reaches values down to −0.48 (Fig. 2c). Already in April, values below −0.35 are reached, so El Niño in boreal winter (year 1–2) is preceded by a cool SD in summer (year 0) (>95% significant using Student's t test).

For comparison, Fig. 2d shows a negative autocorrelation of Niño-3.4 of around −0.45 at lags around 22 months, caused by the cyclicity of ENSO with a mean period of around 4 yr. The SDIex from October (year 0) to August (year 1) is also strongly linked to the state of ENSO in the boreal winter of year 0–1. For SDIex in April, this correlation reaches values of 0.83, while in August–October the correlation to Niño-3.4 at short lags is still up to 0.5. Mature El Niños are known to be
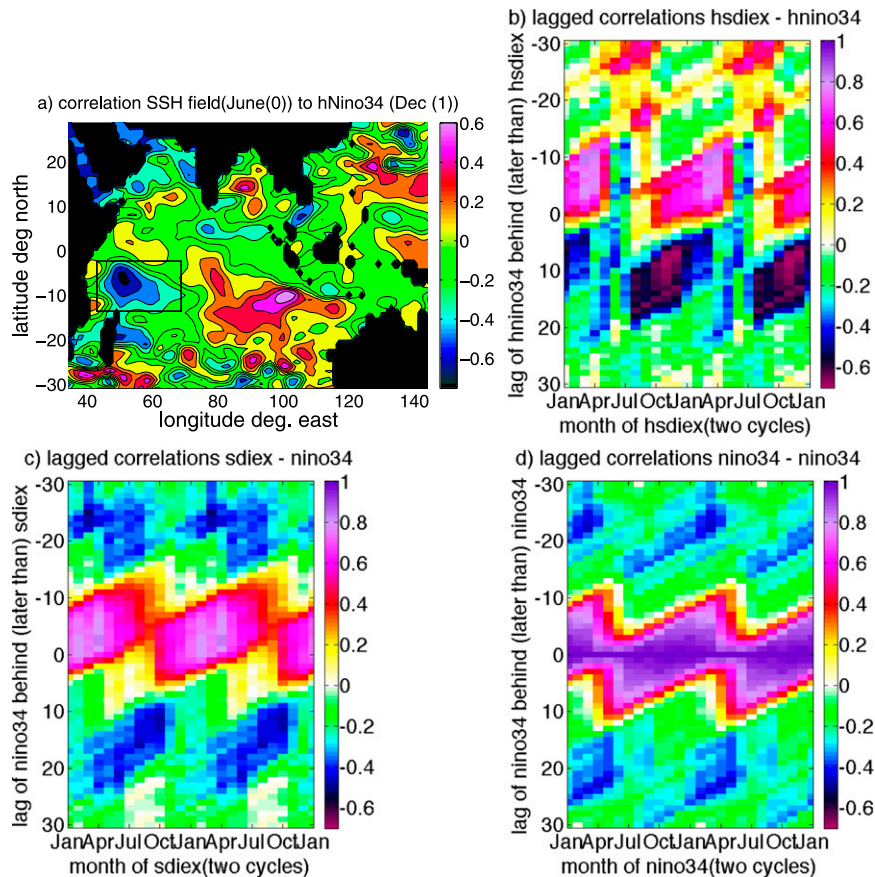
FIG. 2. (a) Correlation of the SSH field in June (year 0) with the hNiño-3.4 index in December (year 1). The black box represents the area in which SDIex and hSDIex are computed. (b) Lagged correlation between hSDIex and hNiño-3.4, where a positive lag (in months) means that hNiño-3.4 is taken at a later time. Month of hSDIex = August and lag = +16 means the time series of hSDIex in August is correlated to hNiño-3.4 16 months later (December of next year). Two annual cycles are shown for convenience. (c) As in (b), but for SDIex and Niño-3.4. (d) As in (b), but for Niño-3.4 correlated to itself. SST data are taken from 1948–2011, while SSH data cover the period of 1993–2012. Using a Student's t test, correlations exceeding 0.25 (0.21) are significant at 95% (90%) confidence for the SST time series, while for the shorter SSH time series (Fig. 2b), correlations should exceed 0.44 (0.38).

associated with anticyclonic winds in the southeastern tropical IO, causing downwelling Rossby waves that arrive in the southwestern IO several months later, lower the thermocline, and hence increase SST (Xie et al. 2002; Schott et al. 2009).

This raises the question whether the negative correlation between SDIex and Niño-3.4 at approximately 1.5-yr lag could be a consequence of ENSO's positive influence on the SD at lags around −5 months, together with ENSO cyclicity. To illustrate this, suppose that Niño-3.4 were perfectly sinusoidal with a period of 4 yr and that SDIex were completely determined by ENSO and would follow Niño-3.4 as a lagged and possibly rescaled copy, for instance, six months later (Fig. 3a). Then a cool SD would appear one-half year after La Niña (black arrows in

Fig. 3a). This cool SD event would automatically be followed by an El Niño after 1.5 years (light blue arrows), without any influence being exerted by the SD on ENSO.

To check whether the SD contains any (linearly) independent information from ENSO, we perform a significance test against the null hypothesis (H0): The negative correlation between SD and Niño-3.4 after 1.5 years is due to the influence of ENSO on the SD and ENSO cyclicity. This is more generally formulated as H0: The correlation between two time series w_2 and w_3 does not significantly differ from what one expects, knowing only their correlations to a third time series v_1; that is, corr(w_2, w_3) is near corr(v_1, w_2) × corr(v_1, w_3).

A more rigorous formulation will follow below. The test to falsify this null hypothesis, henceforth referred to
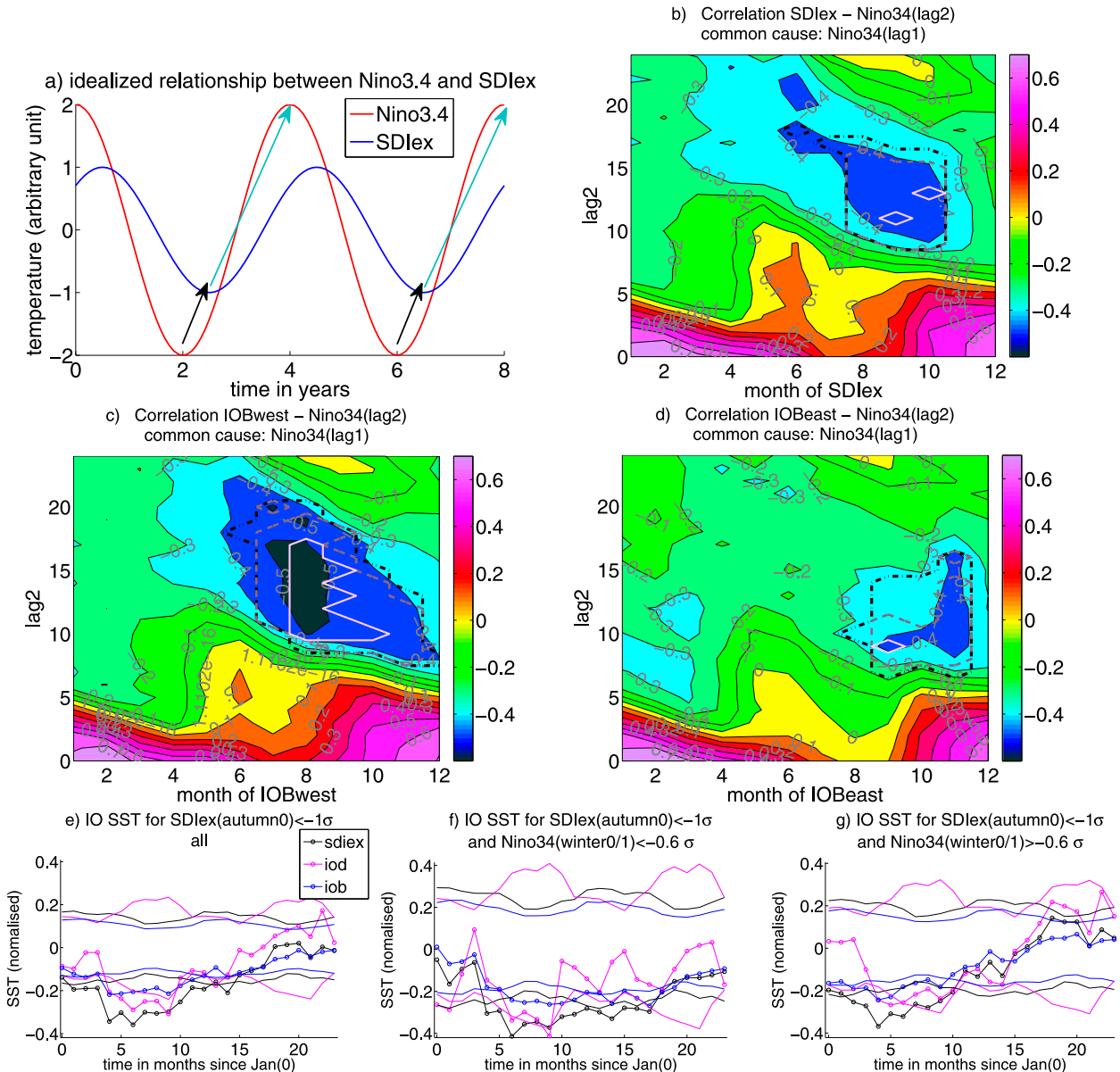
FIG. 3. (a) Illustration of possible influences between Niño-3.4 and SDIex (see text). (b) Results of the common cause test for the correlation of SDIex at a certain calendar month with Niño-3.4 lag_2 months later. Colors denote the true correlation, while the black, gray, and white lines encircle values that are significant at 90%, 95%, and 99% confidence in the common cause test against Niño-3.4 at lag_1 months later than SDIex. The lag_1 values are from $\{-10, -9, \ldots, +4\}$, and the test is only considered passed if the correlation is significant for each value of lag_1. (c),(d) As in (b), but replacing SDIex by IOBwest and IOBeast, respectively. Composites of SDIex (black), DMI (magenta), and BWI (blue) for all years with (e) SDIex[JJASO(0)] $< -1\sigma$ or with the additional constraint that Niño-3.4[Nov(0)–Feb(1)] (f) $< -0.6\sigma$ and (g) $> -0.6\sigma$. Lines with circles show the actual data, while lines with no symbols show the 95% confidence limits. The years 0 in (e) are 1954, 1964, 1984, and 1985 and in (f) are 1965, 1971, 1974, 1989, 1996, and 2004.

as the common cause test, is validated against the output of a conceptual model in the appendix. Let w_2 and w_3 be two time series, for example, SDIex in month m (i.e., one value per year) and Niño-3.4 at a lag later (lag_2), whereas v_1 is the time series of the suspected common cause, for example, Niño-3.4 in month m + lag_1 (lag_1 is typically negative; i.e., v_1 is taken at an

earlier time than w_2). All time series are assumed to have zero mean. Then the test consists of the following steps:

(i) Perform a linear fit of w_2 and w_3 onto v_1 and write $w_2 = av_1 + v_2$ and $w_3 = bv_1 + v_3$, where a and b are linear-fit parameters and v_2 and v_3 the residual time series.

(ii) Reject H0 if 1) v_2 explains a significant percentage of variance of w_3 and 2) v_3 explains a significant percentage of the variance of w_2: This is equivalent to requiring that both corr(v_2, w_3) and corr(v_3, w_2) are significant.

The significance test of corr(v_2, w_3) and corr(v_3, w_2) can be performed as described in section 2a. There is no canonical way to assign a single significance level to the common cause test, which tests two conditions. To be conservative, we consider the test passed at s% significance if both conditions are met at $\geq s$% significance.

As v_2 and v_3 by construction are uncorrelated to v_1, it can be shown that both condition 1 and 2 can never be fulfilled if corr(v_2, v_3) is not significant. In addition, condition 1 will not be fulfilled if w_3 is dominated by v_1 [i.e., std(av_1) $\gg$ std(v_3)], and likewise, condition 2 ensures that w_2 is not dominated by v_1. It can be shown that if corr(v_2, v_3) = 0, then corr(w_2, w_3) = corr(v_1, w_2) $\times$ corr(v_1, w_3).

Note that the common cause test is deliberately allowed to be passed in some cases where corr(w_2, w_3) = 0—namely, if the contribution by v_1 is large but cancelled by the contribution of v_2 and v_3 (i.e., the actual correlation is much weaker than one would expect based on the common cause). One can supplement the common cause test by an ordinary significance test of corr(w_2, w_3) to detect these cases. In our data, this situation never occurred.

To prevent the test passing because of a wrong choice of lag$_1$, values from {−10, −9, . . . , +4} were used. Positive values of lag$_1$ take into account the possibility that the SD anomaly might be caused not by ENSO SST anomalies but by, for example, wind anomalies prior to, and leading to, SST anomalies. A correlation is considered significant only when passing the significance test for all values of lag$_1$. Polynomial rather than linear fits of the w_2 and w_3 data to v_1 at up to fourth order have also been performed but do not improve the fit significantly, so only linear fits are used.

The correlation between SDIex in August–October and Niño-3.4 after roughly 10–15 months is significant against our null hypothesis at 95% confidence; locally even 99% confidence is reached (Fig. 3b). When omitting the very strong 1997/98 El Niño, 95% confidence is still reached (not shown). This indicates that the SD indeed contains independent information on ENSO.

To investigate whether SSH data yield better results than SST—SSH is less influenced by processes other than ocean dynamics, such as surface fluxes—the above analysis was repeated using hSDIex and hNiño-3.4 or hNiño-3 (which is more cyclic than hNiño-3.4). In the common cause test, the resulting correlation between hSDIex (August–September) and hNiño-3 are significant

at 95% confidence (98% for hNiño-3.4; not shown). Correlations can reach values as low as −0.74 (Fig. 2b), but similarly strong values can be reached using SST data in only the years where SSH data are available, so it cannot be concluded that SSH performs better.

To check the relation between SD and IOD or IOBM, the common cause test was repeated with IO indices other than SDIex. For IODwest, BWI (both not shown), or IOBwest (Fig. 3c), slightly stronger correlations are obtained and 99% confidence are reached at more points than for SDIex. For IOBeast (Fig. 3d), significant correlations occur about two months later and weaker than for IOBwest, probably because the cold signal in the IO spreads eastward. IODeast never reaches significant values, and the DMI performs less well than IODwest. Thus, it is the western IO in late boreal summer–autumn that carries the most information about ENSO, though the region of strongest correlation is not confined to the SD.

Annamalai et al. (2005) suggest that a negative autumn IOD (including a cool western IO) does not by itself have a strong impact on the PO because its eastern and western poles are so close that their influence on PO wind cancels. However, Izumo et al. (2015) suggest that a negative IOD is followed by a negative BWI in spring, which influences the PO by creating westerlies there (Santoso et al. 2012; Annamalai et al. 2005). According to Izumo et al. (2015), the IOB-induced westerlies in spring are stronger if there was an IOD in the previous autumn. However, we find that a common cause test between SDIex (autumn year 0) and Niño-3.4 (winter year 1–2) against BWI (spring year 1) as common cause is significant [95% confidence for SDIex in June–October (JJASO) and 99% confidence in August–September (AS); not shown], which suggests that the western IO contains information independent of BWI. Since the BWI (spring year 1) is strongly influenced by Niño-3.4 (winter year 0–1)—Figs. 3e–g suggest that a cool autumn SDIex is only followed by a significant spring BWI in the case of a co-occurring La Niña—this result is in line with Fig. 3b. The mechanism of Izumo et al. (2015) is likely not independent of (a biannual component of) ENSO.

4. Indo-Pacific covarying modes of variability

a. MSSA: Indo-Pacific ENSO modes

To investigate the spatiotemporal patterns of the tropical Indo-Pacific, an MSSA (section 2b) is performed simultaneously to the SST, zonal wind, and burstiness fields. The power spectra (Fig. 4) show (oscillatory pairs of) significant EEOFs. In the data-adaptive test (Fig. 4b), three pairs with periods in the interannual band extend
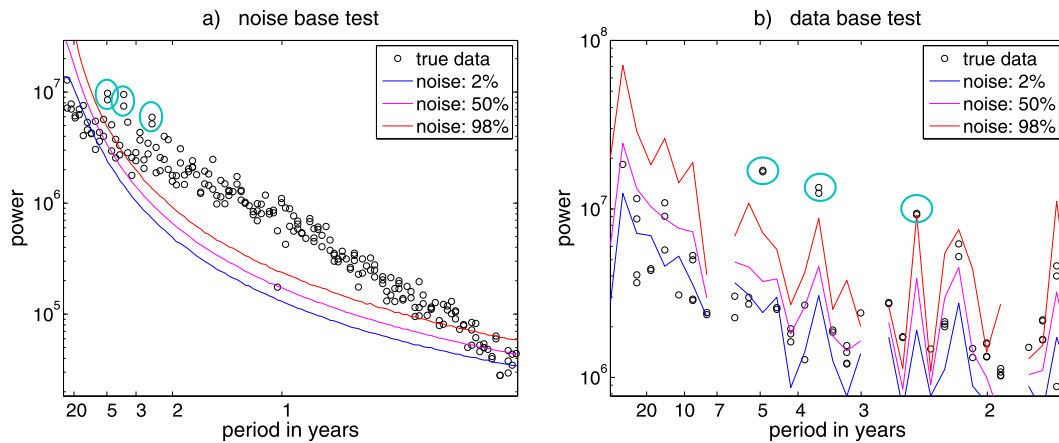
FIG. 4. Spectra of the variance against period in (a) the noise base and (b) the data base test. The black circles correspond to the data, while the red, magenta, and blue lines denote the power under which 98%, 50%, and 2% of the surrogates lie, respectively. The high-frequency parts are cut off from the plots. Significant pairs of EEOFs are marked by blue circles.

above the 98% level: EEOF2 and EEOF3 with a period of 4.9 yr and explaining 9.6% of the variance, EEOF4 and EEOF5 with a period of 3.6 yr and explaining 7.4% of the variance, and EEOF8 and EEOF9 with with a period of 2.5 yr and explaining 5.3% of the variance. At all of these periods there is an enhanced variance also in the noise base test (Fig. 4a) compared to the variances in neighboring frequencies.

Figure 5a shows that the correlation between the sum of the three oscillatory modes and the original (detrended and low-pass filtered) data is high (up to 0.85) in the central-eastern PO and also in most of the IO, particularly the SD (up to 0.68), while correlations in the Atlantic Ocean, the warm pool, and the southeastern IO are much weaker. The sum of the three modes captures all major El Niño and La Niña events, though the asymmetry between warm and cold events is reduced (not shown). Figure 5b shows the standard deviation of several ENSO indices, SDIex, and the east Atlantic Ocean index (AOeast) (see Table 1) as obtained by reconstructing the time series for a certain pair of EEOFs, divided by the value obtained when considering all EEOFs in the reconstruction (this normalization ensures that the relative importance of the contributions from the oscillating pairs can be estimated). The figure also demonstrates that the individual oscillations have stronger signals in the Niño indices and SDIex than in the Atlantic; they represent Indo-Pacific ENSO modes. Figure 5c shows the lag for which the correlation between some SST-based index and Niño-3.4 becomes maximal, divided by the period of the corresponding oscillation. All oscillations found here are dominated by an ENSO-like SST signal in the PO (Figs. 6a,d,g)—that is, a strong oscillation in the eastern and central PO, to which the SST in the western PO is in

antiphase. The normalized standard deviation of SDIex is also high for all three oscillations (Fig. 5b), with SDIex signals lagging Niño-3.4 by approximately 0.04–0.13 periods (Figs. 5c and 6a,d,g), whereas the Atlantic signal is much weaker.

The zonal wind field (Figs. 6b,e,h) has its strongest signal in the eastern IO and western–central PO. For all significant oscillations, SST maxima (minima) in the central-eastern PO are accompanied by westerly (easterly) winds on the equator around 190°E (EEOF2 and EEOF3), 200°E (EEOF4 and EEOF5), or 175°E (EEOF8 and EEOF9), which are nearly in phase with the SST signal, peaking at most 1 month earlier. This wind pattern is typical for ENSO. During the peak of El Niño (La Niña) a patch of easterlies (westerlies) forms in the IO around the equator and 90°E, consistent with the SST difference between the western IO and the Indonesian seas. The wind anomaly moves eastward, temporarily weakening above Indonesia, and reaches the western PO slightly before Niño-3.4 passes through zero. It then rapidly spreads eastward and strengthens along with the SST anomaly forming the next La Niña (El Niño). Wind anomalies propagating from the IO to the PO are consistent with Clarke (2003) and Kug et al. (2010). During and after El Niño (La Niña), a diverging (converging) wind anomaly is thus present above Indonesia, which may help to deplete (build up) the western PO warm pool (Wyrtki 1985; Jin 1997a). A positive WWV anomaly in turn is a precursor to El Niño (Meinen and McPhaden 2000).

The burstiness (Figs. 6c,f,i) is positive (negative) in the PO east of 150°E during El Niño (La Niña), with strongest values occurring at 10°N (not shown). West of 150°E, negative (positive) anomalies are found. During
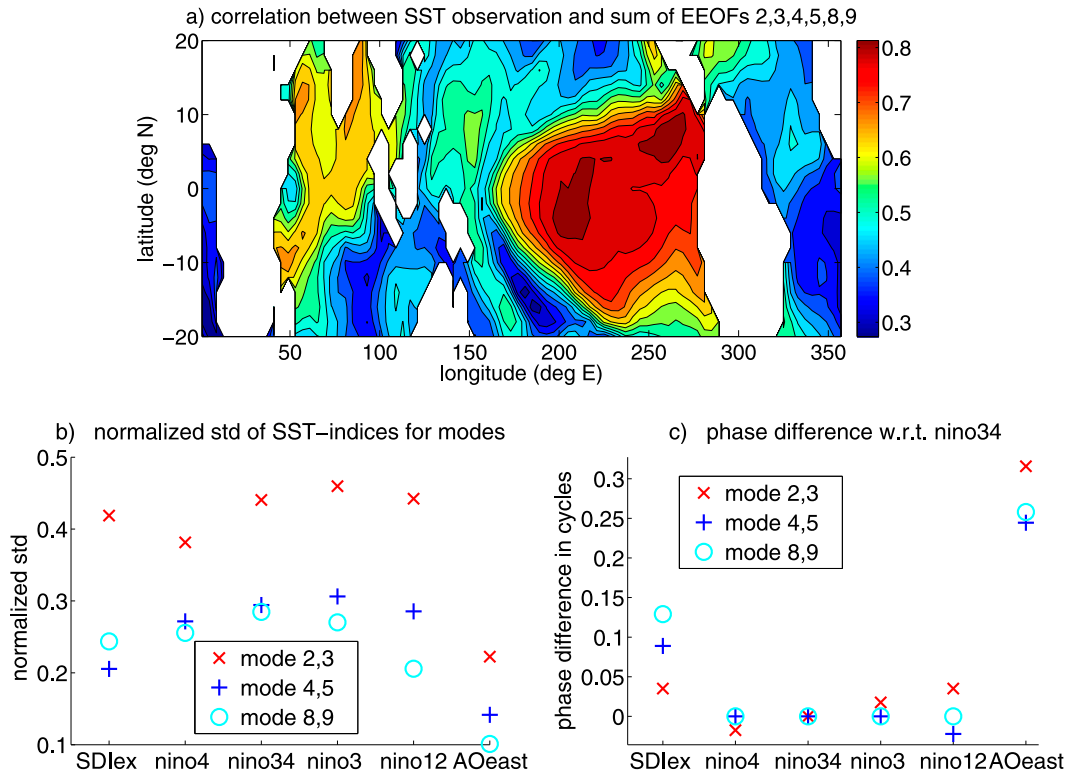
FIG. 5. (a) Correlation between the full SST data used for the MSSA and the reconstructed time series resulting from the three significant MSSA oscillations EEOFs 2 and 3, EEOFs 4 and 5, and EEOFs 8 and 9. (b) Standard deviation of SST-based indices for the three significant oscillations. The values are normalized by the corresponding value obtained by including all EEOFs [e.g., for EEOFs 2 and 3 and Niño-3.4, the plot shows std(Niño-3.4, EEOFs 2 and 3)/std(Niño-3.4, all EEOFs)]. (c) Phase relations of SST-based indices to Niño-3.4. The plot shows the lag for which the correlation between an index I and Niño-3.4 becomes maximal, divided by the period of the corresponding EEOF. A value of $+\frac{1}{4}$ means that I peaks $\frac{1}{4}$ period later than Niño-3.4.

the decay of El Niño (La Niña) the positive (negative) anomaly moves southeastward (meridional propagation component; not shown) and decays, while the negative (positive) one propagates eastward, reaching the western PO before Niño-3.4 becomes negative (positive). High (low) zonal wind variability is thus present in the western PO prior to the onset of El Niño (La Niña), consistent with McPhaden et al. (2006) and Kug et al. (2010), who suggest that strong zonal wind variability is a precursor to El Niño. Western PO burstiness may be influenced by the IO (Izumo et al. 2010a; Wilson et al. 2013).

To test the robustness of the results above, we repeated the MSSA with (i) 30 instead of 70 EOFs, (ii) lag windows of 100 or 140 months, (iii) a low-pass filter with $M = 2$ and $M = 6$ in Eq. (4), and (iv) data only between 40°E and 290°E (i.e., omitting the Atlantic). The results were hardly affected.

Figure 7 shows that the SST evolution in the early stages of El Niño is not the same for all three modes. The early stages of evolution are represented by the moment

where Niño-3.4 passes through zero while increasing (Figs. 7a,d,g) and three (for EEOFs 2 and 3 and EEOFs 4 and 5) or two (EEOFs 8 and 9) months after Niño-3.4 passes through zero (Figs. 7b,e,h). The mature El Niño phase is represented by the moment where Niño-3.4 reaches its maximum (Figs. 7c,f,i). For EEOF2 and EEOF3 (Figs. 7a–c) there is a slight warm anomaly in the western PO when Niño-3.4 switches from negative to positive. South of the equator between Peru and about 225°E, a cool anomaly (remnants of the previous La Niña) is found to the southwest of the warm anomaly. Three months later, the warm anomaly has intensified and spread farther east, and the narrow band along the South American coast south of the equator begins to warm, too. For EEOF4 and EEOF5 (Figs. 7d–f) the evolution is almost the other way around, starting along the Peruvian coast and growing westward. However, the mature El Niño phase looks very similar to that of EEOF2 and EEOF3, with a strong warm anomaly along the cold tongue that extends to about 160°E and the strongest anomalies along the Peruvian coast. For
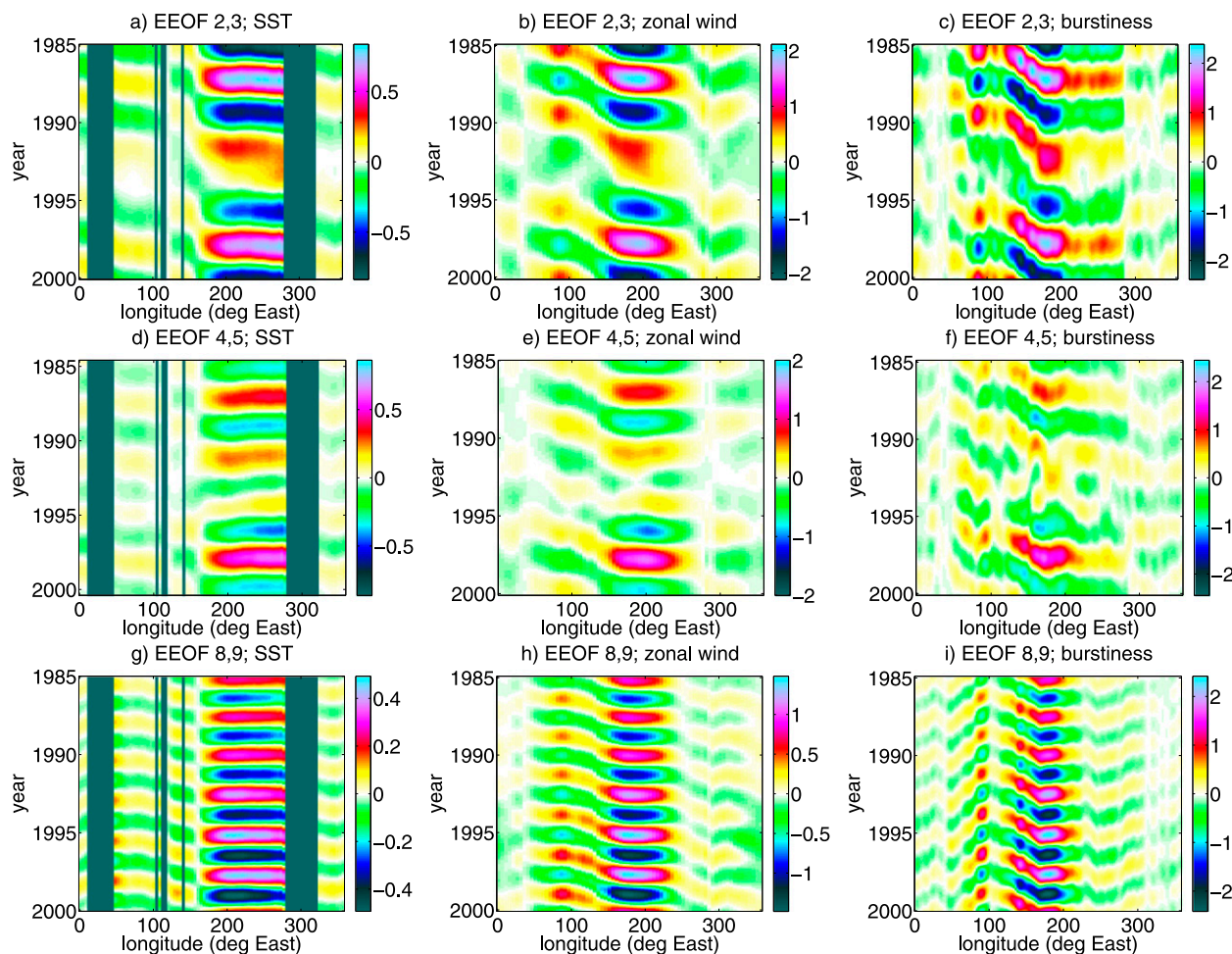
FIG. 6. Hovmöller diagrams of the reconstructed time series of the significant oscillations (a)–(c) EEOFs 2 and 3, (d)–(f) EEOFs 4 and 5, and (g)–(i) EEOFs 8 and 9 obtained by an MSSA of (left) SST, (center) zonal wind, and (right) burstiness. Data are averaged over the region 5°N–5°S and only the years 1985–2000 are shown.

EEOF8 and EEOF9 (Figs. 7g–i) El Niño starts as a warm anomaly in a narrow band along the equator, while cool anomalies (remnants of the previous La Niña) are found poleward of it. The warm anomaly intensifies and broadens poleward, without zonal propagation. The fully grown El Niño is similar to the other modes, except that its maximum lies at 210°E rather than near the coast.

EEOF8 and EEOF9 share some properties with the CP El Niño described in the literature. It is not propagating and it has a shorter period than the other ENSO modes (viz., 2.5 yr). Both findings agree well with those of Kao and Yu (2009), but the spatial pattern of the EEOF8 and EEOF9 El Niño does not resemble the horseshoe pattern found in that paper. However, the CP Niño composites of Kug et al. (2009) and Ashok et al. (2007) do not show a pronounced horseshoe pattern either, but a warm anomaly centered at about

170°W (i.e., 20° farther west than for our EEOF8 and EEOF9).

EEOFs 2 and 3 and EEOFs 4 and 5 represent EP El Niños, of which the former shows eastward initial growth (EPe) and the latter westward growth (EPw). All modes are Indo-Pacific ENSO modes; there are no significant pure PO or pure IO modes.

b. ENSO types and the Seychelles dome

In this subsection a composite analysis is used to investigate whether the ENSO types found in the MSSA—CP, EPe, and EPw—interact in a different way with the SD.

We introduce the shorthand notation $I(m) > \sigma$ to denote that the anomaly of index I in the set of months m for some selected years is larger than the standard deviation σ of I in m over all available years.
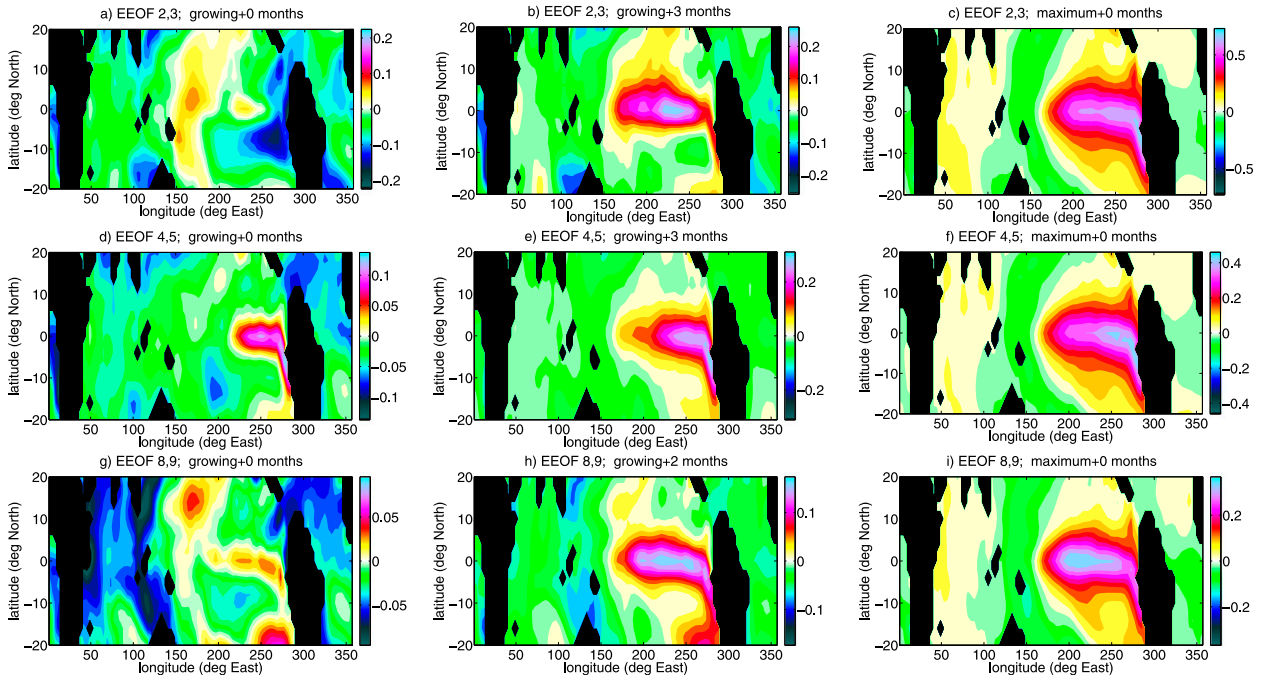
FIG. 7. The development of an El Niño in the three significant oscillations (a)–(c) EEOFs 2 and 3, (d)–(f) EEOFs 4 and 5, and (g)–(i) EEOFs 8 and 9 from the MSSA. For each oscillation, a composite of the SST field is given at three stages of the ENSO cycle: (left) for the moment where Niño-3.4 is increasing and passes through zero, (center) three (for EEOFs 2 and 3 and EEOFs 4 and 5) or two (EEOFs 8 and 9) months later, and (right) for the moment where Niño-3.4 is maximal. Note that the color scale is not the same for all panels.

The El Niños {Niño3.4[Nov(1)–Feb(2)] > 0.9σ}, where, for example, Nov(1) is November (year 1), and so forth, are split into three categories:

1) CP Niños, with EMI[Nov(1)–Feb(2)] > 1.2σ (1968/69, 1994/95, and 2009/10);
2) EPw Niños that are not CP and, in addition, Niño1+2[Apr(1)–Sep(1)] > 1σ (1957/58, 1965/66, 1972/73, and 1997/98); and
3) EPe Niños that are not CP and not EPw (1982/83, 1986/87, 1991/92, and 2002/03).

Note that our concept of westward/eastward growth differs from that of Santoso et al. (2013), who follow the propagation of the peak of El Niño in summer (year 1)–winter (year 1–2) whereas we are concerned with the initial stages of an event. The exact values of the thresholds were chosen to generate roughly equally large groups. EPw events show a warm anomaly in the eastern Pacific during spring and summer (year 1) (Fig. 8b), which is significantly different from zero (95% confidence) and from the other types (90% confidence). In Jan(2), there is no significant difference between EPe and EPw events, but there is between CP and EP events (Fig. 8k); CP events are centered more in the central PO and extend less far to the east. Therefore, sorting the El Niños into CP, EPe, and EPw

events is sensible. It should be noted that the sorting into EPe and CP events is quite sensitive to small changes in the criteria (i.e., events easily change between these groups), whereas the distinction between EPw events and others, which can be made using only Niño-1+2[Apr(1)–Sep(1)], is more robust.

EPw events are preceded by a cool IO anomaly in July–October (year 0) (Fig. 8a), which is significantly different from zero (95% confidence) and is particularly strong in and to the southeast of the SD. EPe events are also preceded by a slight cool IO anomaly, but it is not significant (Fig. 8e). CP events are preceded by a significant warm anomaly around 70°E and cool anomalies to the east and west thereof (Fig. 8i). The cool anomaly around the SD for EPw events is significantly stronger than for EPe and CP events (90% confidence). It is also significantly stronger than for the union of EPe and CP events, so the result that EPw events are preceded by the coolest SD is sensible despite the fact that the distinction between CP and EPe is not very robust. Compared to the union of EPe and CP events, EPw events are preceded by significantly lower (more negative) values of SDIex (confidence of 90% in July–October and 95% in August–September); lower IODwest (confidence of 90% in September–November and 95% in September), IOBwest (confidence of 90% in August–December and
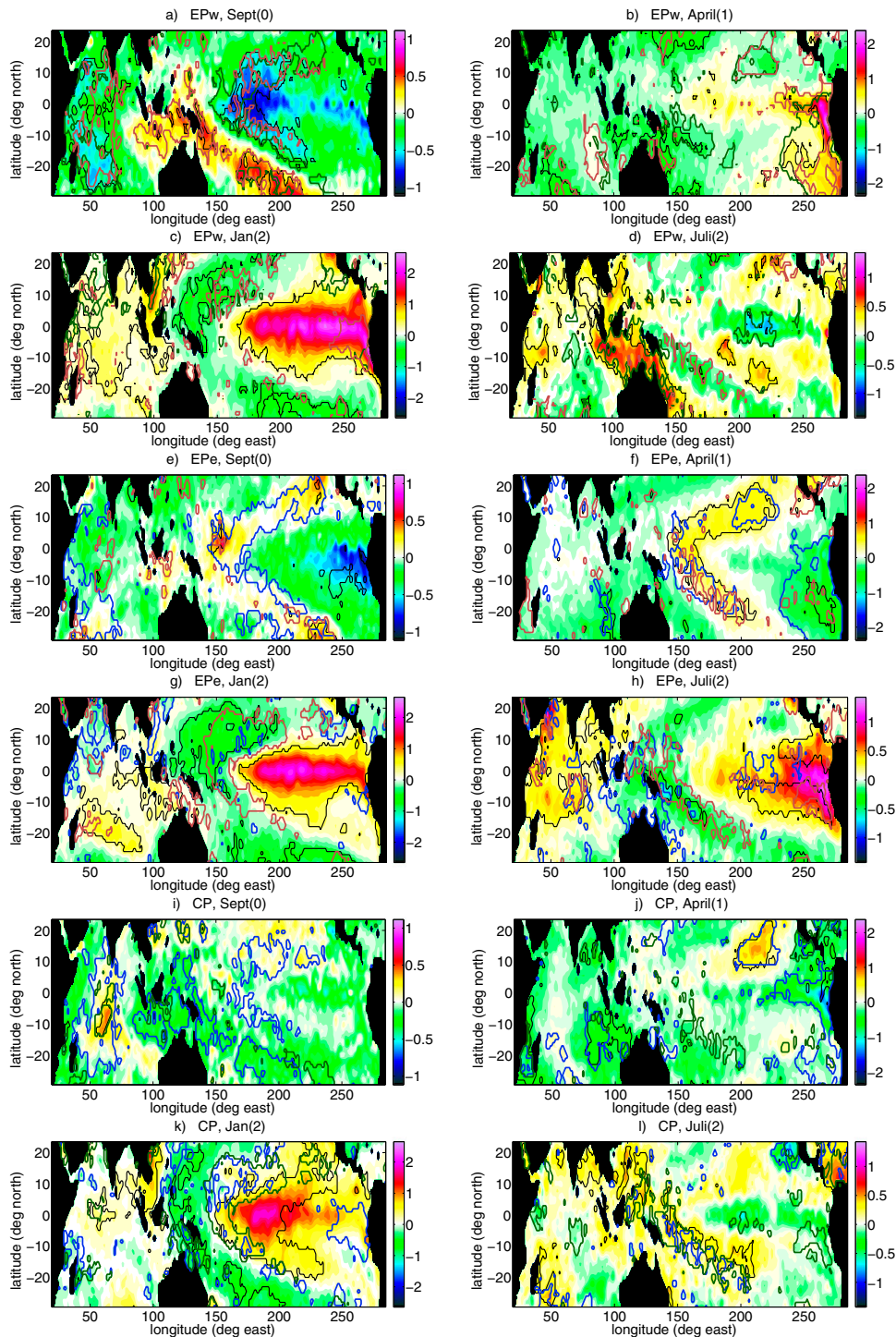
FIG. 8. Composites of the SST field in September (year 0), April (year 1), and January and July (year 2) for (a)–(d) EPw, (e)–(h) EPe, and (i)–(l) CP El Niños. The thin solid black line denotes the 95% confidence level (two tailed) of the corresponding SST field against zero. The thicker red, blue, and green lines mark regions where the SST is different from the CP, EPw, and EPe cases at 90% confidence, respectively.
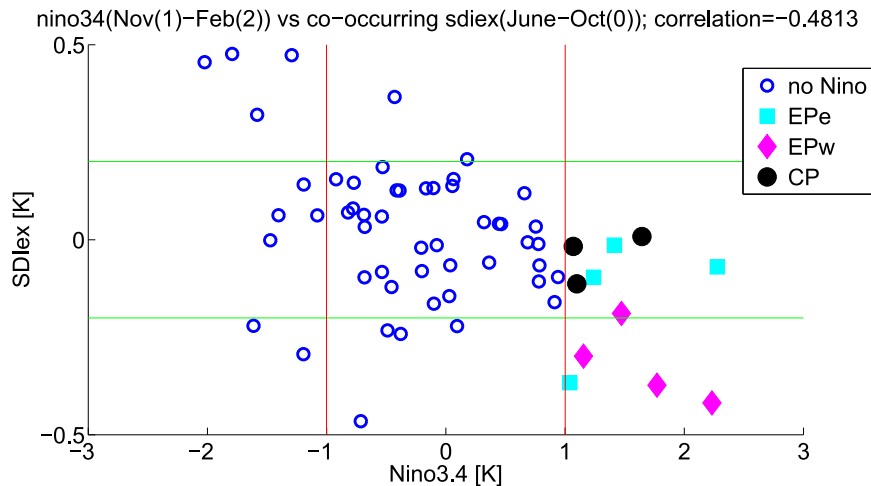
FIG. 9. Scatterplot of SDIex[Aug(0)–Nov(0)] vs Niño-3.4[Nov(1)–Feb(2)]. The El Niño events are marked according to their class as EPe (light blue squares), EPw (pink diamonds), or CP (black-filled circles). The classification is performed as in section 4b. La Niñas are not marked as they cannot properly be categorized. The horizontal green (vertical red) lines are at $\pm 1\sigma$ for SDIex (Niño-3.4).

95% in September–November), and BWI (confidence of 90% in August–December and 95% in September–October); and IOD (confidence of >90% in July, September, and October and 95% in July and September). Figure 9 illustrates that all EPw El Niños are preceded by an autumn (year 0) SDIex below -0.9σ, whereas this is only the case for one EPe and no CP event.

For La Niñas, no criterion could be found that divides the events into a CP and EP type that differ significantly (90% confidence). This is consistent with Kug and Ham (2011). When dividing the La Niñas {i.e., Niño3.4[Nov (1)–Feb(2)] > -1σ} into events with or without an early cooling against the Peruvian coast {threshold: Niño1+2[Apr(1)–Sep(1)] > -0.75σ}, the two groups hardly differ [90% confidence is reached in Mar(1)–Jul(1); for El Niño; the confidence is 98% in Apr(1)–Sep(1)]. No significant differences in the preceding IO indices can be detected. Note that the subdivision into westward- and eastward-growing La Niñas can be expected to be problematic because 1) La Niñas typically have a relatively weak signal in Niño-1+2 and 2) often 2–3 La Niñas occur in a row, so it is hard to distinguish whether a signal in spring–summer belongs to the previous or following event.

All El Niño types are followed by a positive anomaly in Saji et al.'s (1999) BWI (95% confidence) in spring (year 2), so they all cause basinwide warming (not shown); the difference between the ENSO types is not significant. In the case of the EP El Niños, the IO remains warm until late summer (year 2), with a maximum at the SD (Fig. 8). All ENSO types show interaction with the IO at least via the link between ENSO and the following IOBM; hence, it is reasonable that in the MSSA

all significant oscillations (not only the EPw one) have a signal in the IO.

However, a cool western IO event seems to favor EPw El Niños, whereas for La Niñas, a classification into EPe, EPw, and CP events is not useful. Mechanisms by which the western IO can influence ENSO will be discussed in the next section.

5. Evaluation of mechanisms

The results of the previous section suggest that the IO and the PO ENSO signal are strongly linked, which may be due to mutual influence. Since much research has been done on the influence of ENSO on the SD (Xie et al. 2002; section 4.1 of Schott et al. 2009), we will focus here on influences of the SD onto ENSO. As we have seen in section 4a, for all significant MSSA modes during and after a La Niña or cool SD event, zonal winds converge over Indonesia, while later on, westerly winds propagate from the IO to the PO, hinting at an atmospheric bridge mechanism (section 5a). In addition, the burstiness was found to have a positive (negative) anomaly prior to the onset of El Niño (La Niña). These changes in wind variability might be influenced by the IO through a state-dependent noise mechanism (section 5b).

a. Atmospheric bridge

The concept of influence of the IO on the PO transmitted by large-scale atmospheric processes (atmospheric bridge) is more than a decade old (Clarke 2003; Annamalai et al. 2005; Chen and Cane 2008) and has been thought to arise from the IOD (Izumo et al. 2010b),

the IOBM (Santoso et al. 2012), or a combination of both (Izumo et al. 2015). Nevertheless it seems useful to investigate further the link between SD and ENSO because our correlation analysis in section 3 showed that the western IO contains more information on ENSO than the eastern IO. In addition, the influence of the SD and western IO can be linked to the different El Niño types described in section 4.

To identify possible large-scale mechanisms, we made composites of SST and zonal wind for the five years with the strongest negative SDIex anomaly in JJASO(0) between 1948 and 2010. The selected years are 1964, 1971, 1984, 1985, and 1996. The results in Figs. 10a–j are consistent with the MSSA results discussed above, but performing this separate composite analysis allows us to check significance of some relations suggested by the MSSA technique. Figure 10a shows that in July of year 0, the main part of the IO is significantly cooler than normal, with the largest deviation of 0.8 K in the SD region. In the equatorial PO, remnants of a previous La Niña can be seen, surrounded by warmer anomalies (horseshoe pattern; Wang et al. 1999), especially in the southwestern PO under the South Pacific convergence zone. From March to October, the wind to the west of Indonesia is westerly, while to the east of Indonesia, above the western PO, it is easterly (Fig. 10b).

This effect on the PO across the barrier of Indonesia can be explained by the atmospheric bridge mechanism; a cold anomaly in the SD region, extending northward beyond the equator, leads to subsidence in the western IO and, as a Gill-type response (Gill 1980), convection above the warm Indonesia, which causes a westerly anomaly above the IO. The convection above Indonesia is so strong that it also attracts air from the western PO, causing an easterly anomaly there. To check whether the easterly wind anomaly is related to the state of the SD or caused by the La Niña conditions in the PO, we compute the wind field associated to the current state of ENSO (obtained by regressing the zonal wind to Niño-3.4) and subtract this ENSO-induced wind from the composites. The remaining wind $U_r(\mathbf{x}, m)$ at a position $\mathbf{x}$ in month m for a composite over a set Y of N_Y years is thus obtained by

$$U_r(\mathbf{x}, m, Y) = \frac{1}{N_Y} \sum_{i \in Y} U(\mathbf{x}, m, i) - A(\mathbf{x}, m)\, \text{Niño3.4}\,(m, i),$$

(5)

where $U(\mathbf{x}, m, i)$ is the zonal wind at $\mathbf{x}$ in month m and year i, and $A(\mathbf{x}, m)$ is the regression coefficient in $\mathbf{x}$ and m. A running mean over 3 months was applied to the zonal wind prior to computing A and U_r in order to obtain a clearer signal. Throughout the first eight

months of year 0, the easterlies in the equatorial western to central PO are stronger than expected based on the Niño-3.4 values (i.e., $U_r < 0$; Figs. 10k,l). The magnitude of U_r is similar to that of $A \times$ Niño-3.4. However, significance is not very high with only 80% confidence (two tailed). In March, May, and July, 90% is reached, but in June confidence drops below 80%. These results are in line with the atmospheric bridge mechanism but not with a very high confidence.

Easterly winds in the western PO are thought to influence the next year's El Niño by increasing the Pacific warm water volume (Izumo et al. 2010b), which in turn is a prerequisite for an El Niño event (Jin 1997a; Meinen and McPhaden 2000). We find that the WWV is indeed negatively correlated to previous SDIex. This correlation is strongest (-0.73) for SDIex in November and WWV around five months later, but values below -0.45 (significant at 98% confidence according to a two-tailed Student's t test) are found throughout the year. However, the influence of ENSO on the WWV is also strong. Therefore we test the significance of the lagged correlation between SDIex and WWV by using the common cause test of section 3, with Niño-3.4 as the common cause. It turns out that the correlation between SDIex (August–November) and WWV (around five months later) is significantly stronger than expected from ENSO's influence on SDIex and WWV (95% confidence; figure not shown). Using IODwest instead of SDIex gives very similar results. IODeast never gives correlations significant at 90% confidence. The full DMI yields significant correlations (95% confidence) slightly earlier than IODwest and SDIex, namely for DMI in June–October. This suggests that a cool western IO is indeed followed by an enhanced WWV after a few months. This result cannot be explained by the IOBM-based mechanism proposed by Santoso et al. (2012) and Izumo et al. (2015), which only involves westerlies over the PO.

In October, the easterly anomaly over the western PO starts moving southeastward and decaying (not shown), while the westerlies above the IO shift eastward and reach the western PO in Dec(0)–Jan(1) (see Fig. 10d). Meanwhile, the horseshoe pattern warm anomaly in the southwestern PO has spread eastward toward the end of year 0 and then moves northward along the South American coast, weakening (Figs. 10c,e). In April of year 1, the water near the Peruvian coast starts warming (Fig. 10e), reaching significant values in May; in June the anomaly starts growing westward along the equator (Fig. 10g). The westerly winds move to the central PO and increase along with the SST anomaly (Figs. 10f,h,j), hinting at a Bjerknes feedback. The eastward propagation of the wind anomalies in winter–spring
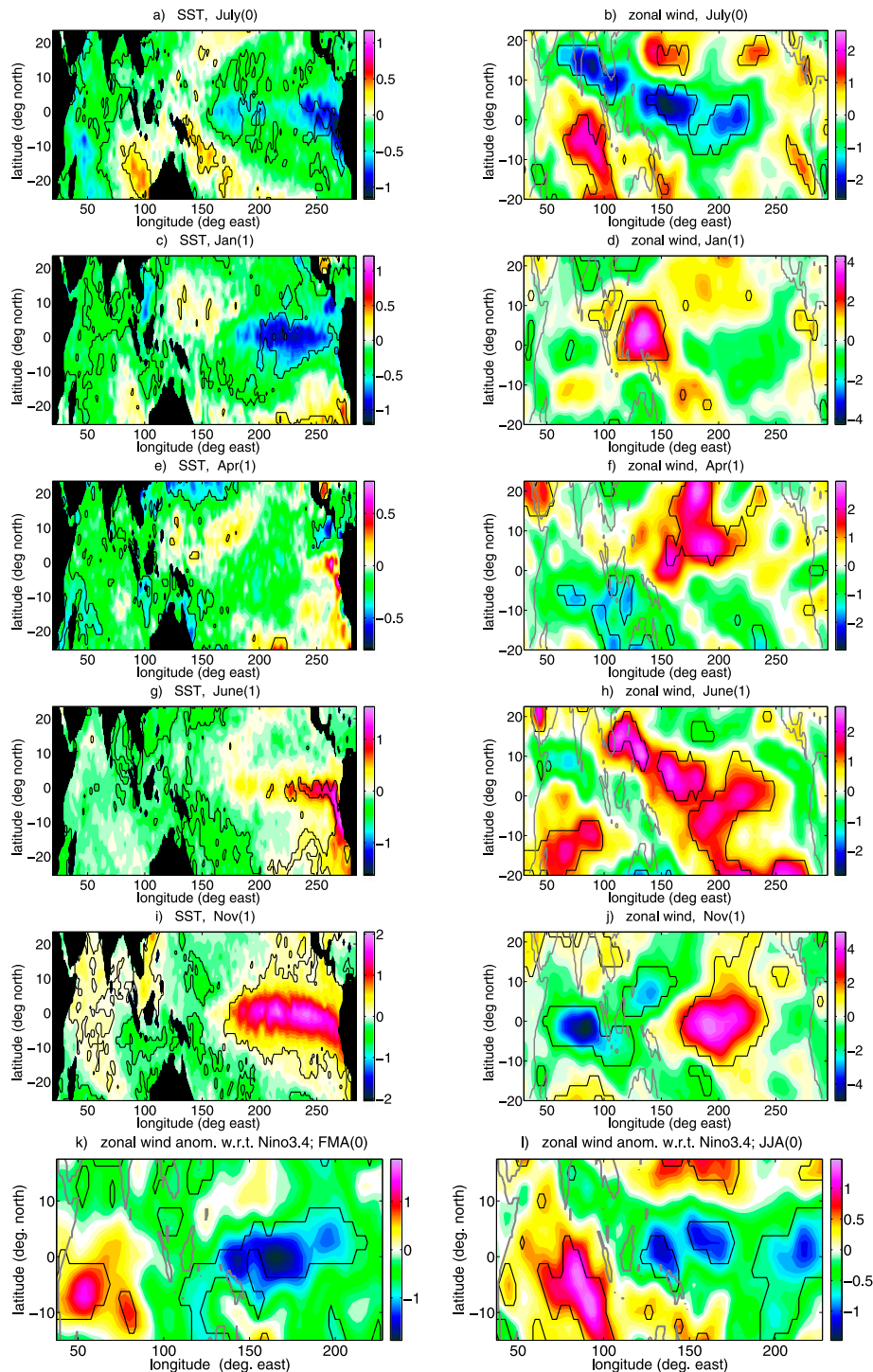
FIG. 10. (a)–(j) Composites of the five coolest SD events in JJASO of year 0. The panels show (left) SST (K) and (right) zonal wind (m s^{-1}) anomalies, for the months (a),(b) July of year 0, (c),(d) January year 1, (e),(f) April year 1, (g),(h) June year 1, and (i),(j) November year 1. Black lines mark the 90% confidence limits. (k),(l) Composites of the zonal wind (m s^{-1}) in the five coolest SD events minus the zonal wind associated with the ongoing La Niña [i.e., $U_r(\mathbf{x}, m)$ as defined in the text]. A 3-month running mean has been applied to the zonal wind. The plots show the situation in FMA and JJA of year zero. Black lines mark the 80% confidence limits (two tailed). Note that the color scale differs for each panel.

(year 1) and the following increase is consistent with the MSSA results.

Despite the fact that this eastward propagation of winds has long been known (Barnett 1984; Clarke 2003), to our knowledge the underlying mechanism is still uncertain. Gill (1983) and Barnett et al. (1991) suggest mechanisms by which coupled SST–wind anomalies can propagate eastward on the PO, but they depend on the local background state. Latif and Barnett (1995) conclude that the eastward propagation on global scales around the tropics is coincidental, while White and Cayan (2000) describe a ''global ENSO wave'' possibly based on SST–atmosphere feedbacks. Numerical experiments by Izumo et al. (2015) suggest that a switch from IOD to IOBM in late autumn (year 0) could cause westerlies above the western PO. IOD–IOBM transitions co-occur with La Niña in winter (year 0–1) (see section 3).

The processes described above may favor a westward-moving EP El Niño. First, EP El Niños need a large WWV to develop (Meinen and McPhaden 2000), while Kao and Yu (2009) suggest that CP events have a smaller vertical extent and are more dominated by winds and SST advection than by thermocline processes. Yu and Kim (2010) find that CP events can take place in a recharged, neutral, or discharged WWV state. Hence, an increase in WWV associated with a cool SD would favor EP events but should not influence CP events. Second, eastward-growing and CP El Niños are initiated later in the year than westward-growing El Niños. Harrison and Schopf (1984) attributed the eastward propagation of the 1982/83 El Niño to the fact that westerly wind forcing occurred in boreal summer (not spring) of 1982—that is, at a time when the climatological zonal SST gradient in the central PO is strongly negative and hence anomalous eastward currents can cause strong zonal advection in the central PO. The westward-growing El Niño of 1997/98, for which thermocline depth and upwelling played a vital role (Vialard et al. 2001), started in spring. In the composites in Fig. 10d it can be seen that a westerly anomaly reaches the western PO as early as Jan(1), where it can induce downwelling Kelvin waves leading to a warming at the Peruvian coast in spring.

A similar analysis for the five warmest SD years in June–October (year 0) (i.e., years 1961, 1972, 1983, 1987, and 1998) yields a significant La Niña signal in winter (year 1–2) with 95% confidence (the El Niño signal following a cool SD also reaches 95% confidence). The cold anomaly starts being significant in Apr(1) and extends from Peru to 160°E without initial westward growth. It is not possible to detect westerly winds in the western PO in summer–autumn (year 0), which are significantly stronger than what one would expect from the Niño-3.4 signal at the same time.

b. State-dependent noise

The IO might also influence ENSO by altering the characteristics of short-scale atmospheric processes above the PO. By short-scale noise we mean processes of time scales much smaller than that of ENSO itself but long enough to influence ENSO (i.e., of roughly intraseasonal time scales). In the MSSA we have seen that burstiness anomalies propagate from the IO into the PO, with positive anomalies in the western PO during the onset of El Niño.

To investigate possible effects of the SD/IOD on the burstiness, we regress the burstiness in February–April (FMA) onto the SDIex in previous summer–autumn. Direct influence by the previous ENSO is removed by taking a bilinear regression:

$$\tilde{B}(\mathbf{x}, t_1) = a(\mathbf{x})\tilde{S}(t_2) + b(\mathbf{x})\tilde{N}(t_3) + R, \qquad (6)$$

where $\tilde{B}(\mathbf{x}, t_1)$ is the normalized burstiness in location $\mathbf{x}$ and time t_1 (FMA of year 1), $\tilde{S}(t_2)$ is the normalized SDIex at time t_2 [within Jun(0)–Nov(0)], and $\tilde{N}$ is the normalized Niño-3.4 index at time t_3 [Dec(0)]. Normalization is performed pointwise by dividing by the standard deviation {e.g., $\tilde{B}(\mathbf{x}, t_1) = B(\mathbf{x}, t_1)/\sigma[B(\mathbf{x})]$}. The coefficients a and b are local regression coefficients and R is the residual; because of the normalization, a and b are from $[-1, 1]$. To investigate the influence of the burstiness on ENSO, we also regressed Niño-3.4 in Sep(1)–Jan(2) to the previous FMA burstiness field.

Figure 11a shows that El Niño in December is preceded by a positive burstiness anomaly around the equator at 140°–200°E in FMA. On the other hand, the regression of the burstiness onto SDIex in the previous July (Fig. 11b) is negative in a region around 2.5°S, 140°E, overlapping with the region of positive regression to Niño-3.4. These results are consistent with the MSSA of section 4a and robust against shifting lags by 1–2 months or using January–March (JFM) or March–May (MAM) burstiness. They suggest a possible causal link between a cool SD and El Niño via enhanced burstiness.

To investigate the relation between SD, intraseasonal westerlies, and ENSO further, and to understand the mechanisms underlying the burstiness, an MSSA of the 5-day zonal wind field between 20°N and 20°S is performed. In the prefiltering step the first 50 EOFs are included, accounting for 80% of the variance. The length of the lag window is 24 pentads. The results are robust against a 20% variation in the number of EOFs included or the length of the time window.

We obtain two significant oscillatory pairs that both span the IO and PO: EEOFs 4 and 5 and EEOFs 8 and 9. The Hovmöller plots in Figs. 12a,b show that the phase velocity in the IO and western PO is about 60° (15 days)$^{-1}$ ≈ 5 m s^{-1}
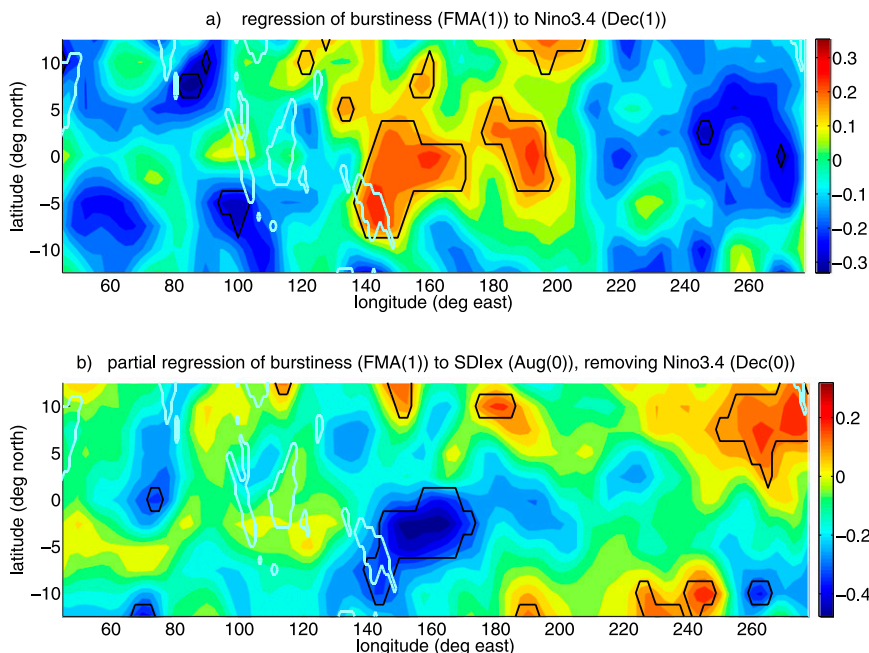
FIG. 11. Regressions between the burstiness field and various SST-based indices. Indices and local burstiness time series are normalized to unit standard deviation. Thick black lines denote the 95% confidence level. Shown are (a) regression of Niño-3.4 in December to the burstiness in previous FMA and (b) partial regression of burstiness in FMA onto SDIex in previous July, removing Niño-3.4 in previous December.

and increases in the central-eastern PO. The PCs of the first pair have a period of about 53 days, while those of the second pair have a dominant period of about 80 days with a relatively strong first harmonic (40 days). About 70% of the power of this mode lies at periods longer than 55 days, the local minimum of the power spectrum (Fig. 12d). Both the dominant periods observed and the behavior of the phase velocity are characteristic of the MJO.

The relationship between the two oscillating pairs and ENSO/IO variability is checked by correlating the variance of the corresponding PCs over blocks of 3 months (henceforth referred to as the pair's running variance) to Niño-3.4, SDIex, and DMI. Correlations between the running variance and monthly SST-based indices are significant at 95% confidence when outside approximately ±0.25, as was checked using the technique from section 2a. The running variance of EEOF4 and EEOF5 has hardly any significant correlation to ENSO, DMI, or SDIex (not shown). However, there is a significant negative correlation between the running variance of EEOF8 and EEOF9 in October–December (OND) and April–June (AMJ) and SDIex in the previous summer–autumn (lags from −5 to −10 months), which is strongest (−0.34) for the running variance in JFM and FMA (Fig. 13). In addition, the running variance of the PCs in December–February (DJF) and May–July (MJJ) is positively

correlated to the following autumn–winter Niño-3.4 (lags from around +3 to +12 months), with values above 0.45 being reached in FMA–AMJ. Correlations between running variance in FMA–AMJ and the following SDIex (i.e., at lags around 12 months) are significantly positive, too. Applying the common cause test from section 3 confirms that the negative correlation between SDIex in July–October and EEOF8 and EEOF9 running variance in the following DJF and AMJ is significant (90% confidence) against the null hypothesis that the correlation is caused by a possible influence of ENSO on SDIex and the running variance of EEOF8 and EEOF9 (not shown). Using DMI instead of SDIex yields slightly weaker correlations, which are not significant at 90% confidence in the common cause test. While the western pole of the DMI yields results very similar to those using SDIex (not shown), the eastern pole never yields significant correlations at negative lags.

These findings suggest that modifications of long-period MJO variability by the western IO might at least partly explain the interannual variability in the burstiness in boreal winter–spring (the time where the interannual variability of mode EEOF8 and EEOF9 variance is strongest; see Fig. 13a). This result is in line with Wilson et al. (2013), who demonstrated from observations that the MJO is slightly strengthened (considerably
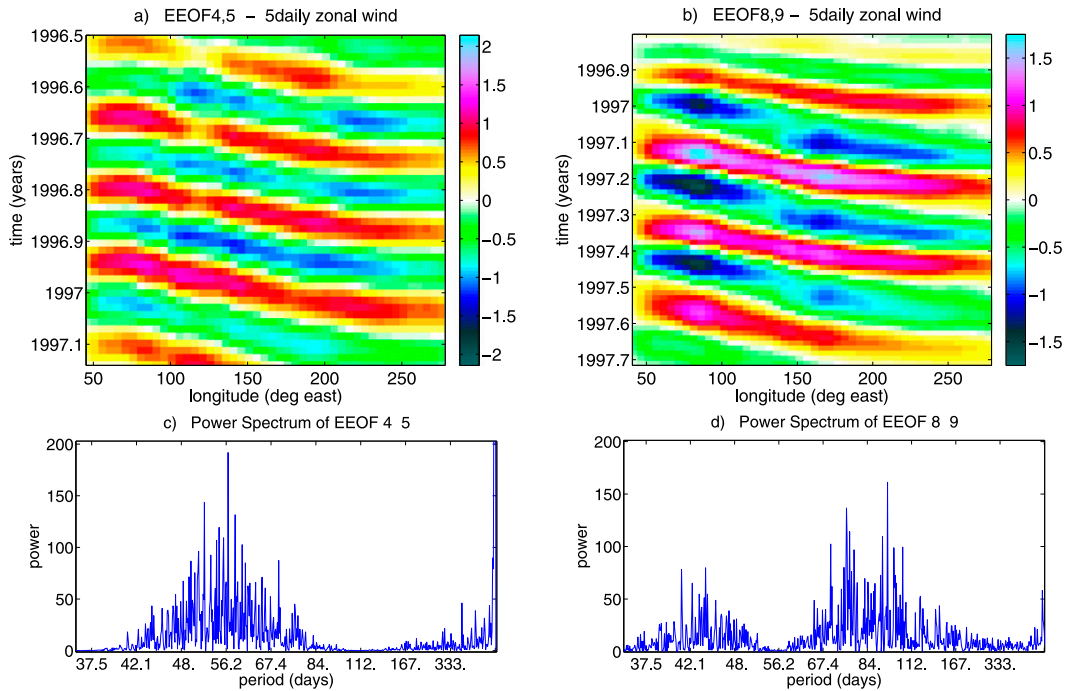
FIG. 12. Hovmöller plots of (sections of) the reconstructed time series of (a) EEOFs 4 and 5 and (b) EEOFs 8 and 9 of the pentad zonal wind, averaged over the latitude band 5°N–5°S. Power spectra of the PCs belonging to (c) EEOFs 4 and 5 and (d) EEOFs 8 and 9.

weakened) in negative (positive) IOD years and link these observations to increased air moisture content, wind convergence, and reduced sea level pressure above Indonesia in years following a negative IOD. Izumo et al. (2010a) find that the low-frequency part (period > 55 days) of the boreal winter MJO signal is weakened

after a positive IOD, possibly due to the IOD's influence on the mean state of the atmosphere or enhanced sea–atmosphere coupling in the SD region during negative IOD (i.e., cool SD and/or shallow thermocline). Intraseasonal westerlies such as those provided by the MJO can generate anomalous eastward currents,
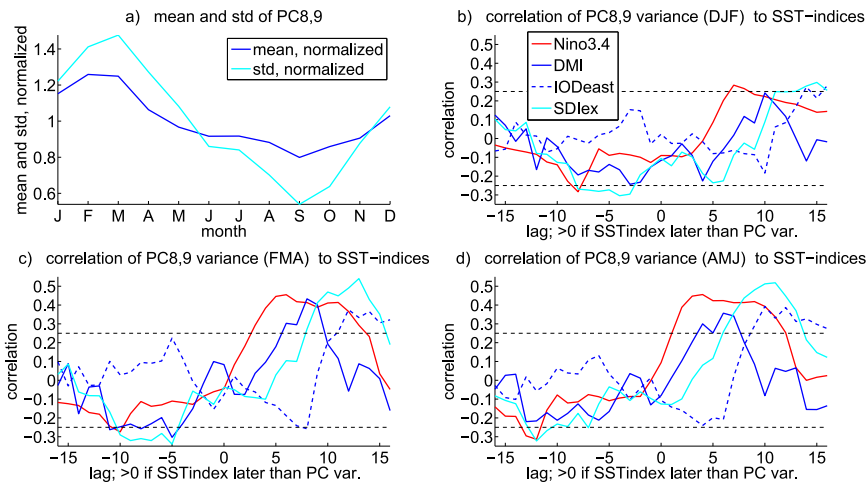

FIG. 13. (a) Seasonal cycle of the running variance of PCs 8 and 9. The dark blue line is the mean over all years of the running variance in a 3-month block centered at a certain calendar month; the bright blue line is the standard deviation over all years. (b)–(d) Correlation of PC8 and PC9 running variances to Niño-3.4 (red), DMI (solid dark blue), IODeast (dashed dark blue), and SDIex (light blue). The PC running variance is given for months (b) DJF, (c) FMA, and (d) AMJ. The black dashed horizontal lines indicate the 95% confidence limits.
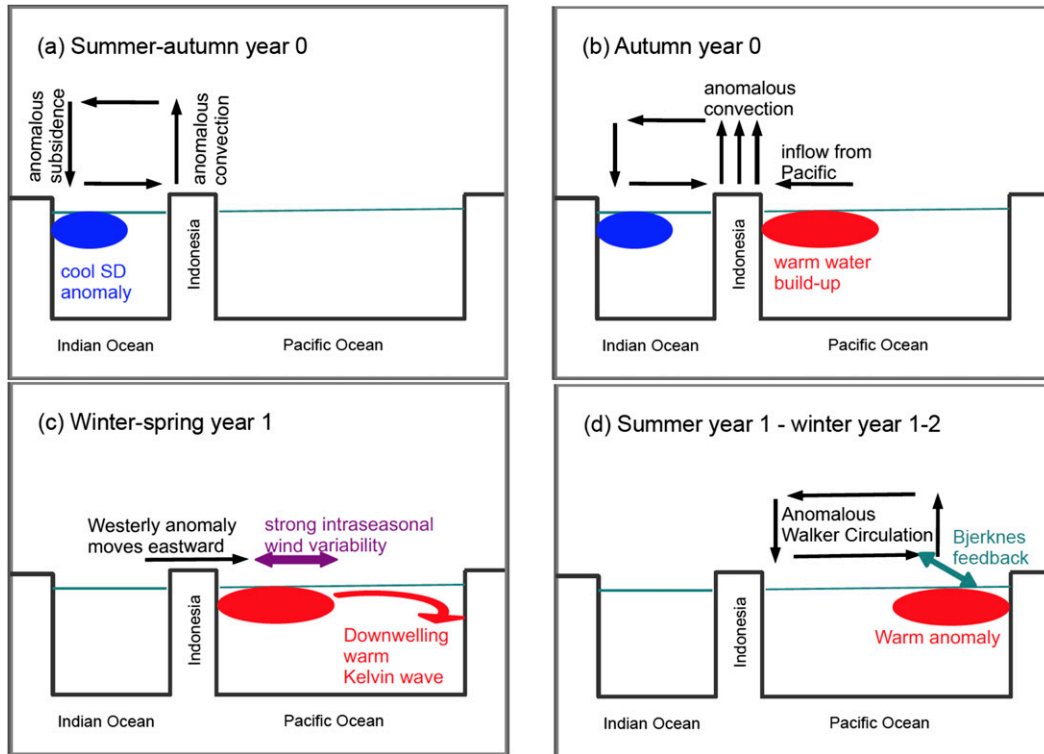
FIG. 14. The combined atmospheric bridge and state-dependent noise mechanism by which a cool SD may affect El Niño development. In summer–autumn of year 0, (a) a cool SD leads to enhanced convection and hence converging winds above Indonesia, which help create a (b) strong warm pool in the western PO. During winter–spring of year 1, anomalous westerlies propagate toward the western PO and the zonal wind variability in the western PO is anomalously high, so (c) intraseasonal spells of westerly winds can initiate a downwelling Kelvin wave early in the year, which leads to (d) a strong warming in the eastern PO and the development of a westward-growing EP El Niño during the next summer–autumn.

leading to zonal SST advection, and intraseasonal downwelling Kelvin waves that help lower the eastern PO thermocline (Zhang 2005; Kessler et al. 1995; McPhaden et al. 2006).

Our analysis not only confirms earlier results with different techniques (MSSA, common cause test) but suggests that one mode—the long-period MJO mode EEOF8 and EEOF9—provides a link between SD in summer–autumn (year 0) and El Niño in autumn–winter (year 1). In addition, we find that it is the western IO, rather than the eastern IO, which influences the MJO. Finally we remark that the negative correlation between EEOF8 and EEOF9 running variance and the previous SDIex peaks earlier than the positive correlation between running variance and the later Niño-3.4, though there is some overlap for running variance around FMA. So the SD-induced impact of the MJO on ENSO occurs early during the time where ENSO is sensitive to such a forcing. As discussed in section 5a, such an early westerly wind forcing is likely to stimulate a westward-growing EP El Niño.

6. Summary, discussion, and conclusions

A multichannel singular spectrum analysis (MSSA) of SST, zonal wind, and burstiness (intraseasonal wind variability) of the tropical oceans yields three significant modes, all of which show an ENSO signal in the PO and a strong SST variability in the western IO but only weak signals in the Atlantic. No pure PO or IO mode is found, suggesting that the Pacific ENSO cycle and the IO closely interact.

The Pacific ENSO signals in the two MSSA modes with periods of 4.9 and 3.6 yr (EEOFs 2 and 3 and EEOFs 4 and 5) are strongest in the eastern PO (Niño-3–Niño-1+2 region). In the former mode the SST anomaly starts in the central PO and spreads eastward (EPe event), while in the latter, the anomaly grows from the South American coast to the west (EPw). The third mode (EEOFs 8 and 9) has a period of 2.5 yr and the ENSO signal is strongest around 150°W and shows no zonal propagation. This nonpropagating behavior and a maximum away from the South American coast are properties
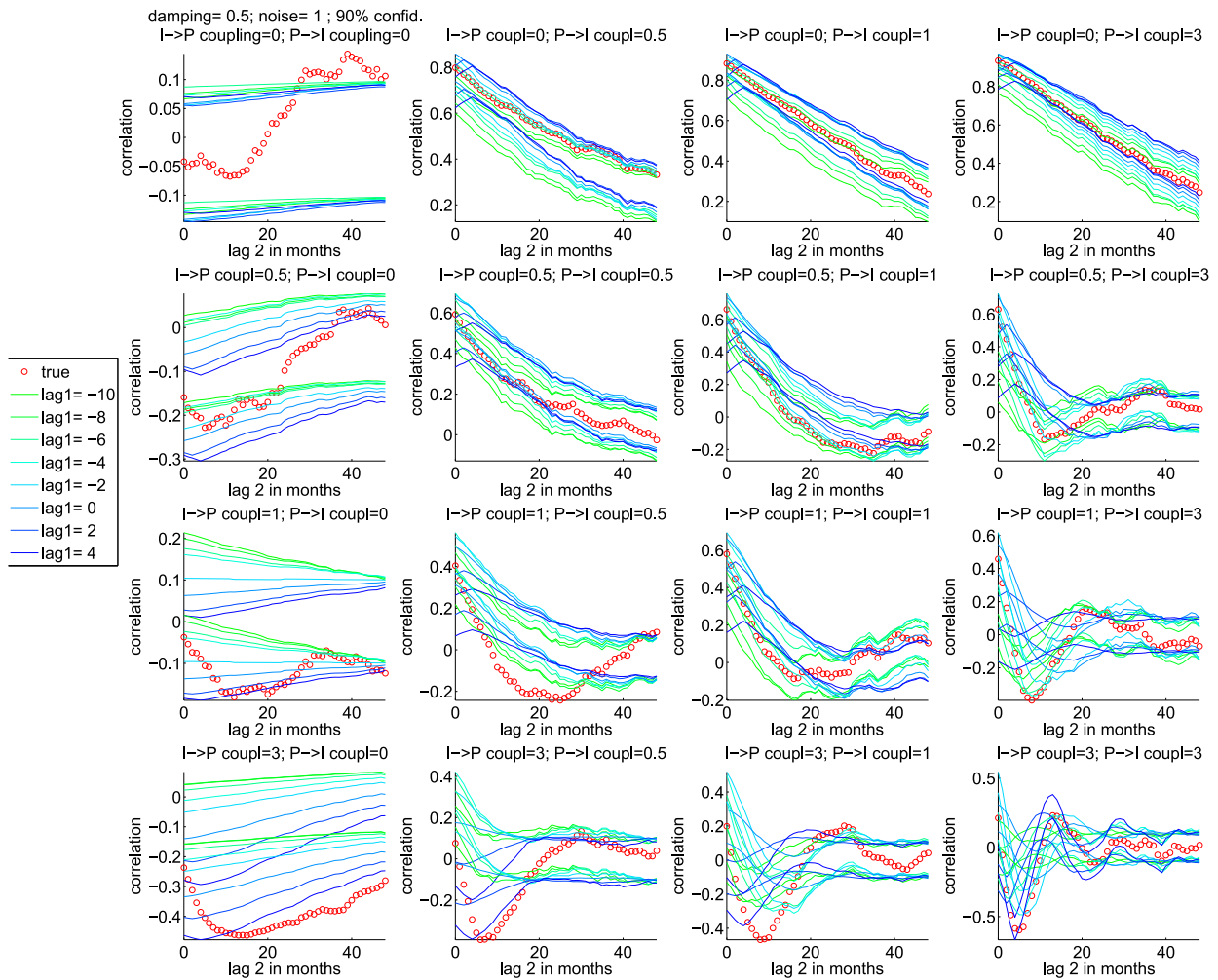
FIG. A1. Results of the common cause test for 250 years of toy model data, with $k_{damp} = 0.5$ and $k_{noise} = 1$. The factor k_{IP} (scaling the influence onto the Indian from the Pacific Ocean; see appendix) increases from left to right and k_{PI} increases from top to bottom; both range from 0 to 3. The red circles denote the true correlation between T_I and T_P at lag_2 (positive when T_P is later), while the green and blue lines denote the regions within which 90% of the surrogate data lies, for various values of lag_1 (in months; negative when the T_P value used as common cause is earlier than T_I).

of CP El Niños, though a typical CP El Niño peaks still farther west. In all significant modes, El Niño (La Niña) is followed by a warm (cool) SD 2–4 months later, which reflects the influence of ENSO on the western IO (Xie et al. 2002), but might also feed back on ENSO.

In particular, the SDIex in summer–autumn is negatively correlated to Niño-3.4 approximately 1.5 years later. This correlation is significant against the null hypothesis that it is caused by ENSO's influence on the SD and ENSO's cyclicity. The various ENSO types are differently influenced by the SD. A composite analysis shows that EPw El Niños are preceded by cool western IO anomalies that are significantly stronger than for other El Niño types. La Niñas cannot be sorted into EPe, EPw, and CP events.

Based on these results, two mechanisms were investigated by which the SD may influence ENSO (Fig. 14). In the atmospheric bridge mechanism, subsidence over a cool SD leads to westerlies over the IO and enhanced convection above Indonesia, causing easterlies over the western PO. These are stronger than expected on the ground of influence from the decaying La Niña still present in the PO (80% confidence) and favor the buildup of a strong warm pool. Indeed, the SD in August–November is significantly negatively correlated to the WWV around five months later (95% confidence against the null hypothesis that the correlation is caused by ENSO influence on SD and WWV). The enhanced warm pool can be activated during the next spring–summer, when the patch of westerly winds has

propagated from the IO to the PO. The mechanism for this eastward propagation remains an open issue. In the state-dependent noise mechanism, a cool SD in summer leads to an enhanced wind variability during the next early spring, as was confirmed by regressing FMA (year 1) burstiness onto SDIex in August (year 0). An MSSA over 5-day zonal wind data suggests that interannual variability in the low-frequency part of the MJO might be a source of the burstiness variation. Intraseasonal wind variability in the western PO is known to force intraseasonal Kelvin waves that may induce El Niño development (Kessler et al. 1995; McPhaden et al. 2006).

Both mechanisms favor the development of westward-growing EP El Niños. First, because EP El Niños need a sufficient WWV to develop, while CP El Niños do not and second, because both the westerly wind anomaly that propagates into the western PO and the enhanced burstiness after a cool SD event in summer–autumn (year 0) reach the western PO in late winter to early spring (year 1). At this time of the year, westerly wind forcing is more likely to create SST anomalies in the eastern PO through downwelling Kelvin waves than advection-induced anomalies in the central PO because the zonal SST gradient in the central PO is typically weak in spring. The atmospheric bridge and state-dependent noise mechanisms might be interrelated since large-scale westerlies as found in the western PO from spring (year 1) onward and zonal wind variability might reinforce each other (Kug et al. 2010).

From observational data it cannot be decided which mechanism is more relevant and in fact other mechanisms might also play a role, such as variability in the Indonesian Throughflow induced by SSH anomalies in the southeastern IO (Yuan et al. 2011, 2013). Modeling studies are necessary to disentangle cause and consequences, especially concerning influences on the WWV, and investigate important issues such as how the wind anomalies propagate from the IO to the PO on interannual time scales and how this might influence the burstiness.

The results presented here strongly suggest that the interannual variability in the IO and PO is quite coherent. Although there is no one-to-one relationship between the Seychelles dome SST variations and ENSO, a better understanding of this connection will provide a valuable additional ingredient for ENSO prediction at longer lead times and for understanding the behavior of ENSO on longer time scales. It would be interesting to investigate whether the frequent occurrence of CP El Niños in recent decades (Ashok et al. 2007) is linked to the strong warming of the southwestern IO since the 1970s. If so, the southwestern IO temperature trends might also influence the changes in ENSO under global warming.

APPENDIX

Validation of the Common Cause Test

To validate the common cause test, we apply it to data generated by the conceptual recharge oscillator model in Jansen et al. (2009):

$$\frac{d}{dt}\begin{pmatrix} T_P \\ h_P \\ T_I \end{pmatrix} = \begin{pmatrix} -2\gamma_P & \omega_0 & c_{PI} \\ -\omega_0 & 0 & c_{h,PI} \\ c_{IP} & 0 & -2\gamma_I \end{pmatrix} \begin{pmatrix} T_P \\ h_P \\ T_I \end{pmatrix} + \begin{pmatrix} \eta_{TP} \\ \eta_{hP} \\ \eta_{TI} \end{pmatrix},$$

where T_P, h_P, and T_I are the SST in the (eastern) PO, the PO thermocline depth, and the IO SST, respectively; γ_P and γ_I denote the SST damping in the PO and IO, respectively; ω_0 regulates the coupling between PO SST and thermocline, while c_{PI} and c_h,PI describe the influence of IO SST onto PO SST and thermocline, respectively, and c_{IP} describes the influence of PO SST onto IO SST. The parameters are fitted from observations and are provided in Jansen et al. (2009). We generated time series for a model with adapted coefficients:

$$\frac{d}{dt}\begin{pmatrix} T_P \\ h_P \\ T_I \end{pmatrix} = \begin{pmatrix} -2k_{\text{damp}}\gamma_P & \omega_0 & k_{PI}c_{PI} \\ -\omega_0 & 0 & k_{PI}c_{h,PI} \\ k_{IP}c_{IP} & 0 & -2k_{\text{damp}}\gamma_I \end{pmatrix} \begin{pmatrix} T_P \\ h_P \\ T_I \end{pmatrix}$$
$$+ k_{\text{noise}}\begin{pmatrix} \eta_{TP} \\ \eta_{hP} \\ \eta_{TI} \end{pmatrix},$$

where k_{damp} and k_{noise}, the factors controlling damping and noise strength, are $\in \{0.5, 1, 2\}$ and k_{PI} (k_{IP}), the factor controlling the influence on the PO (IO) exerted by the IO (PO), is $\in \{0, 0.3, 0.5, 1, 2, 3\}$. In Fig. A1, results are given for $k_{\text{damp}} = 0.5$ and $k_{\text{noise}} = 1$.

For all values of k_{damp}, k_{noise}, and k_{IP}, increasing k_{PI} clearly makes the correlations more significant, while increasing k_{IP} has no systematic influence on significance. The passing of the test for some lags with $k_{IP} = k_{PI} = 0$ is an artifact of this particular noise realization. This suggests that the test is capable of detecting influence from the IO on the PO in the presence of ENSO cyclicity and ENSO influence on the IO.

REFERENCES

Allen, M. R., and A. W. Robertson, 1996: Distinguishing modulated oscillations from coloured noise in multivariate datasets. *Climate Dyn.*, **12**, 775–784, doi:10.1007/s003820050142.

——, and L. A. Smith, 1996: Monte Carlo SSA: Detecting irregular oscillations in the presence of colored noise. *J. Climate*, **9**, 3373–3404, doi:10.1175/1520-0442(1996)009<3373:MCSDIO>2.0.CO;2.

Annamalai, H., S. P. Xie, J. P. McCreary, and R. Murtugudde, 2005: Impact of Indian Ocean sea surface temperature on developing El Niño. *J. Climate*, **18**, 302–319, doi:10.1175/JCLI-3268.1.

Ashok, K., S. K. Behera, S. A. Rao, H. Weng, and T. Yamagata, 2007: El Niño Modoki and its possible teleconnection. *J. Geophys. Res.*, **112**, C11007, doi:10.1029/2006JC003798.

AVISO/SSALTO, 2014: MSLA heights in delayed time. Accessed November 2014. [Available online at http://www.aviso.altimetry.fr/en/data/products/sea-surface-height-products/global/msla-h.html.]

Barnett, T. P., 1984: Interaction of the monsoon and Pacific trade wind system at interannual time scales. Part III: The tropical band. *Mon. Wea. Rev.*, **112**, 2388–2400, doi:10.1175/1520-0493(1984)112<2388:IOTMAP>2.0.CO;2.

——, M. Latif, E. Kirk, and E. Roeckner, 1991: On ENSO physics. *J. Climate*, **4**, 487–515, doi:10.1175/1520-0442(1991)004<0487:OEP>2.0.CO;2.

Chen, D., and M. A. Cane, 2008: El Niño prediction and predictability. *J. Comput. Phys.*, **227**, 3625–3640, doi:10.1016/j.jcp.2007.05.014.

Clarke, A. J., 2003: Improving El Niño prediction using a space-time integration of Indo-Pacific winds and equatorial Pacific upper ocean heat content. *Geophys. Res. Lett.*, **30**, 1399, doi:10.1029/2002GL016673.

Gill, A. E., 1980: Some simple solutions for heat-induced tropical circulation. *Quart. J. Roy. Meteor. Soc.*, **106**, 447–462, doi:10.1002/qj.49710644905.

——, 1983: The 1982–83 climate anomaly in the equatorial Pacific. *Nature*, **306**, 229–234, doi:10.1038/306229a0.

Ham, Y. G., J. S. Kug, and J. Y. Park, 2013: Two distinct roles of Atlantic SSTs in ENSO variability: North tropical Atlantic SST and Atlantic Niño. *Geophys. Res. Lett.*, **40**, 4012–4017, doi:10.1002/grl.50729.

Harrison, D. E., and P. S. Schopf, 1984: Kelvin-wave-induced anomalous advection and the onset of surface warming in El Niño events. *Mon. Wea. Rev.*, **112**, 923–933, doi:10.1175/1520-0493(1984)112<0923:KWIAAA>2.0.CO;2.

Izumo, T., S. Masson, J. Vialard, C. de Boyer Montégut, S. K. Behera, G. Madec, K. Takahashi, and T. Yamagata, 2010a: Low and high frequency Madden–Julian oscillations in austral summer: Interannual variations. *Climate Dyn.*, **35**, 669–683, doi:10.1007/s00382-009-0655-z.

——, and Coauthors, 2010b: Influence of the state of the Indian Ocean dipole on the following year's El Niño. *Nat. Geosci.*, **3**, 168–172, doi:10.1038/ngeo760.

——, J. Vialard, H. Dayan, M. Lengaigne, and I. Suresh, 2015: A simple estimation of equatorial Pacific response from windstress to untangle Indian Ocean dipole and basin influences on El Niño. *Climate Dyn.*, 1–22, doi:10.1007/s00382-015-2700-4.

Jansen, M. F., D. Dommenget, and N. S. Keenlyside, 2009: Tropical atmosphere–ocean interactions in a conceptual framework. *J. Climate*, **22**, 550–567, doi:10.1175/2008JCLI2243.1.

Jin, F. F., 1997a: An equatorial ocean recharge paradigm for ENSO. Part I: Conceptual model. *J. Atmos. Sci.*, **54**, 811–829, doi:10.1175/1520-0469(1997)054<0811:AEORPF>2.0.CO;2.

——, 1997b: An equatorial ocean recharge paradigm for ENSO. Part II: A stripped-down coupled model. *J. Atmos. Sci.*, **54**, 830–847, doi:10.1175/1520-0469(1997)054<0830:AEORPF>2.0.CO;2.

Kalnay, E., and Coauthors, 1996: The NCEP/NCAR 40-Year Reanalysis Project. *Bull. Amer. Meteor. Soc.*, **77**, 437–471, doi:10.1175/1520-0477(1996)077<0437:TNYRP>2.0.CO;2.

Kao, H. Y., and J. Y. Yu, 2009: Contrasting eastern-Pacific and central-Pacific types of ENSO. *J. Climate*, **22**, 615–632, doi:10.1175/2008JCLI2309.1.

Keen, R. A., 1982: The role of cross-equatorial tropical cyclone pairs in the Southern Oscillation. *Mon. Wea. Rev.*, **110**, 1405–1416, doi:10.1175/1520-0493(1982)110<1405:TROCET>2.0.CO;2.

Kessler, W. S., M. J. McPhaden, and K. M. Weickmann, 1995: Forcing of intraseasonal Kelvin waves in the equatorial Pacific. *J. Geophys. Res.*, **100**, 10 613–10 632, doi:10.1029/95JC00382.

Kleeman, R., 2008: Stochastic theories for the irregularity of ENSO. *Philos. Trans. Roy. Soc. London*, **366A**, 2509–2524, doi:10.1098/rsta.2008.0048.

Kug, J. S., and Y. G. Ham, 2011: Are there two types of La Nina? *Geophys. Res. Lett.*, **38**, L16704, doi:10.1029/2011GL048237.

——, F. F. Jin, and S. I. An, 2009: Two types of El Niño events: Cold tongue El Niño and warm pool El Niño. *J. Climate*, **22**, 1499–1515, doi:10.1175/2008JCLI2624.1.

——, K. P. Sooraj, T. Li, and F. F. Jin, 2010: Precursors of the El Niño/La Niña onset and their interrelationship. *J. Geophys. Res.*, **115**, D05106, doi:10.1029/2009JD012861.

Larkin, N. K., and D. E. Harrison, 2005: On the definition of El Niño and associated seasonal average U.S. weather anomalies. *Geophys. Res. Lett.*, **32**, L13705, doi:10.1029/2005GL022738.

Latif, M., and T. P. Barnett, 1995: Interactions of the tropical oceans. *J. Climate*, **8**, 952–964, doi:10.1175/1520-0442(1995)008<0952:IOTTO>2.0.CO;2.

Madden, R. A., and P. R. Julian, 1971: Detection of a 40–50 day oscillation in the zonal wind in the tropical Pacific. *J. Atmos. Sci.*, **28**, 702–708, doi:10.1175/1520-0469(1971)028<0702:DOADOI>2.0.CO;2.

McPhaden, M. J., X. Zhang, H. H. Hendon, and M. C. Wheeler, 2006: Large scale dynamics and MJO forcing of ENSO variability. *Geophys. Res. Lett.*, **33**, L16702, doi:10.1029/2006GL026786.

Meinen, C. S., and M. J. McPhaden, 2000: Observations of warm water volume changes in the equatorial Pacific and their relationship to El Niño and La Niña. *J. Climate*, **13**, 3551–3559, doi:10.1175/1520-0442(2000)013<3551:OOWWVC>2.0.CO;2.

Met Office, 2012: Hadley Centre Sea Ice and Sea Surface Temperature data set (HadISST). [Available online at http://www.metoffice.gov.uk/hadobs/hadisst/.]

Mitchell, J. M., B. Dzeerdzeevskii, H. Flohn, W. L. Hofmeier, H. H. Lamb, K. N. Rao, and C. C. Wallen, 1966: Climatic change. WMO Tech. Note 79, 79 pp.

Neelin, J. D., D. S. Battisti, A. C. Hirst, F. F. Jin, Y. Wakata, T. Yamagata, and S. E. Zebiak, 1998: ENSO theory. *J. Geophys. Res.*, **103**, 14 261–14 290, doi:10.1029/97JC03424.

NOAA/OAR/ESRL PSD, 2014: NCEP/NCAR Reanalysis 1: Summary. Accessed February 2014. [Available online at http://www.esrl.noaa.gov/psd/data/gridded/data.ncep.reanalysis.html.]

NOAA/PMEL Tropical Atmosphere Ocean Project, 2014: Upper ocean heat content and ENSO. Accessed November 2014.

[Available online at http://www.pmel.noaa.gov/tao/elnino/wwv/.]

Philander, S. G., 1990: El Niño, La Niña, and the Southern Oscillation. Academic Press, 289 pp.

Plaut, G., and R. Vautard, 1994: Spells of low-frequency oscillations and weather regimes in the Northern Hemisphere. J. Atmos. Sci., **51**, 210–236, doi:10.1175/1520-0469(1994)051<0210:SOLFOA>2.0.CO;2.

Rayner, N. A., D. E. Parker, E. B. Horton, C. K. Folland, L. V. Alexander, D. P. Rowell, E. C. Kent, and A. Kaplan, 2003: Global analyses of sea surface temperature, sea ice, and night marine air temperature since the late nineteenth century. J. Geophys. Res., **108**, 4407, doi:10.1029/2002JD002670.

Saji, N. H., B. N. Goswami, P. N. Vinayachandran, and T. Yamagata, 1999: A dipole mode in the tropical Indian Ocean. Nature, **401**, 360–363.

Santoso, A., M. H. England, and W. Cai, 2012: Impact of Indo-Pacific feedback interactions on ENSO dynamics diagnosed using ensemble climate simulations. J. Climate, **25**, 7743–7763, doi:10.1175/JCLI-D-11-00287.1.

——, S. McGregor, F. F. Jin, W. Cai, H. M. England, S. I. An, M. J. McPhaden, and E. Guilyardi, 2013: Late-twentieth-century emergence of the El Niño propagation asymmetry and future projections. Nature, **504**, 126–130, doi:10.1038/nature12683.

Schott, F. A., S. P. Xie, and J. P. J. McCreary, 2009: Indian Ocean circulation and climate variability. Rev. Geophys., **47**, RG1002, doi:10.1029/2007RG000245.

Tozuka, T., T. Yokoi, and T. Yamagata, 2010: A modeling study of interannual variations of the Seychelles dome. J. Geophys. Res., **115**, C04005, doi:10.1029/2009JC005547.

Vialard, J., C. Menkes, J. P. Boulanger, P. Delecluse, E. Guilyardi, M. J. McPhaden, and G. Madec, 2001: A model study of oceanic mechanisms affecting equatorial Pacific sea surface temperature during the 1997–98 El Niño. J. Phys. Oceanogr., **31**, 1649–1675, doi:10.1175/1520-0485(2001)031<1649:AMSOOM>2.0.CO;2.

Wang, C., R. H. Weisberg, and J. I. Virmani, 1999: Western Pacific interannual variability associated with the El Niño-Southern

Oscillation. J. Geophys. Res., **104**, 5131–5149, doi:10.1029/1998JC900090.

Webster, P. J., A. M. Moore, J. P. Loschnigg, and R. R. Leben, 1999: Coupled ocean–atmosphere dynamics in the Indian Ocean during 1997–98. Nature, **401**, 356–360, doi:10.1038/43848.

White, W. B., and D. R. Cayan, 2000: A global El Niño-Southern Oscillation wave in surface temperature and pressure and its interdecadal modulation from 1900 to 1997. J. Geophys. Res., **105**, 11 223–11 242, doi:10.1029/1999JC900246.

Wilson, E. A., A. L. Gordon, and D. Kim, 2013: Observations of the Madden Julian oscillation during Indian Ocean dipole events. J. Geophys. Res. Atmos., **118**, 2588–2599, doi:10.1002/jgrd.50241.

Wyrtki, K., 1985: Water displacements in the Pacific and the genesis of El Nino cycles. J. Geophys. Res., **90**, 7129–7132, doi:10.1029/JC090iC04p07129.

Xie, S. P., H. Annamalai, F. A. Schott, and J. P. J. McCreary, 2002: Structure and mechanisms of south Indian Ocean climate variability. J. Climate, **15**, 864–878, doi:10.1175/1520-0442(2002)015<0864:SAMOSI>2.0.CO;2.

Yu, J. Y., and S. T. Kim, 2010: Three evolution patterns of central-Pacific El Niño. Geophys. Res. Lett., **37**, L08706, doi:10.1029/2010GL042810.

Yuan, D., J. Wang, T. Xu, P. Xu, Z. Hui, X. Zhao, Y. Luan, W. Zheng, and Y. Yu, 2011: Forcing of the Indian Ocean dipole on the interannual variations of the tropical Pacific Ocean: Roles of the Indonesian Throughflow. J. Climate, **24**, 3593–3608, doi:10.1175/2011JCLI3649.1.

——, H. Zhou, and X. Zhao, 2013: Interannual climate variability over the tropical Pacific Ocean induced by the Indian Ocean dipole through the Indonesian Throughflow. J. Climate, **26**, 2845–2861, doi:10.1175/JCLI-D-12-00117.1.

Zebiak, S. E., and Coauthors, 2015: Investigating El Niño-Southern Oscillation and society relationships. Wiley Interdiscip. Rev.: Climate Change, **6**, 17–34, doi:10.1002/wcc.294.

Zhang, C., 2005: Madden-Julian oscillation. Rev. Geophys., **43**, RG2003, doi:10.1029/2004RG000158.